International Journal of Pharmaceutical Sciences and Drug Research

[ISSN: 0975-248X; CODEN (USA): IJPSPP]

journal home page : http://ijpsdronline.com/index.php/journal

Research Article

Docking-Guided Identification of Natural Urease Inhibitors Against *Helicobacter pylori*: Integrated ADME, Molecular Dynamics, and DFT Investigations

Keshav[1], Manpreet Kaur[1], Ajmer Singh Grewal[2*]

[1]*Department of Pharmaceutical Chemistry, Amar Shaheed Baba Ajit Singh Jujhar Singh Memorial College of Pharmacy, Bela, Ropar, Punjab, India*
[2]*Guru Gobind Singh College of Pharmacy, Yamuna Nagar, Haryana, India*

ARTICLE INFO

Article history:
Received: 13 June, 2026
Revised: 04 July, 2026
Accepted: 10 July, 2026
Published: 30 July, 2026

Keywords:
Helicobacter pylori, Urease Inhibitors, Natural Products, ADME Prediction, Molecular Docking, Sphaeranthanolide.

DOI:
10.25004/IJPSDR.2026.180403

ABSTRACT

Helicobacter pylori is a Gram-negative, microaerophilic bacterium implicated in the development of chronic gastritis, peptic ulcer disease, gastric adenocarcinoma, and MALT lymphoma. The increasing frequency of resistance to antibiotics and treatment failures related to conventional therapies has created an urgent need for the novel discovery of anti-*H. pylori* agents. Urease, a key virulence factor responsible for bacterial survival in the acidic gastric environment, represents an attractive molecular target for therapeutic intervention. The present study aimed to identify potential natural urease inhibitors through a docking-guided screening approach. A total of 126 phytoconstituents from medicinal plants possessing anti-*H. pylori* activity were selected and subjected to *in-silico* evaluation. Of the screened compounds, 92 satisfied the selected drug-likeness criteria and were subsequently investigated through molecular docking against *H. pylori* urease. Docking analysis identified several compounds with notable binding affinity toward urease. Among them, sphaeranthanolide exhibited the highest binding interaction (-7.6 kcal/mol), followed by (+)-catechin (-7.5 kcal/mol), scopoline, epicatechin, and (+)-hardwickiic acid (-7.4 kcal/mol). Detailed interaction analysis revealed the involvement of key active-site residues, including Asp362, Arg338, Gly279, Ala169, Glu222, His221, and Asp223, through hydrogen bonding and hydrophobic interactions. Based on its superior docking results, sphaeranthanolide was selected for further MD simulation and DFT calculation studies. A 100 ns MD simulation confirmed the structural stability of the sphaeranthanolide-urease complex, with persistent interactions maintained throughout the simulation period. DFT calculations demonstrated favorable electronic characteristics, with HOMO and LUMO energies of -11.018 eV and -7.130 eV, respectively, and a HOMO-LUMO energy gap of 3.888 eV. Overall, the integrated application of ADME prediction, molecular docking, MD simulation, and DFT analysis identified sphaeranthanolide as a promising urease inhibitor and lead-potential molecule for the development of novel anti-*H. pylori* agents. The significance findings provide a scientific basis for future experimental validation and further optimization of natural product-derived urease inhibitors.

INTRODUCTION

As a microaerophilic, Gram-negative bacterium, *Helicobacter pylori* specifically colonizes the gastric mucosa, affecting nearly half of the global population. Persistent infection with *H. pylori* is strongly linked with chronic gastritis, peptic ulcer diseases, mucosa-associated lymphoid tissue (MALT) lymphoma, and gastric adenocarcinoma, rendering it one of the most clinically significant human pathogens globally.[1-3] The International Agency for Research on Cancer (IARC) has categorized

***Corresponding Author:** Dr. Ajmer Singh Grewal

Address: Guru Gobind Singh College of Pharmacy, Yamuna Nagar, Haryana, India

Email ✉**:** ajmergrewal2007@gmail.com

Tel.: 91-9416700430

Relevant conflicts of interest/financial disclosures: The authors declare that the research was conducted in the absence of any commercial or financial relationships that could be construed as a potential conflict of interest.

H. pylori as a Group I carcinogen due to its established role in gastric carcinogenesis.[3] Current eradication regimens primarily rely on amalgams of antibiotics, proton pump inhibitors, and bismuth-containing compounds. Although these therapies have substantially improved clinical outcomes, their effectiveness has progressively declined owing to increasing antibiotic resistance, treatment-related adverse effects, poor patient compliance, and frequent therapeutic failures.[4,5] Resistance to routinely prescribed antibiotics, including clarithromycin, metronidazole, and levofloxacin, has emerged as a major global concern, emphasizing the urgent need for alternative therapeutic strategies.[6] Among the numerous virulence factors produced by *H. pylori*, urease plays a pivotal role in bacterial survival and colonization within the highly acidic gastric environment. Urease represents a nickel-reliant metalloenzyme that catalyzes the hydrolysis of urea into ammonia and carbon dioxide, generating a localized neutral microenvironment that protects the bacterium from gastric acidity.[7] The enzyme possesses a unique dodecameric structure consisting of UreA and UreB subunits arranged as a $[(\alpha\beta)_3]_4$ complex and contains a highly conserved binuclear nickel active site essential for catalytic activity.[8] Given that urease is crucial for *H.pylori* pathogenesis as well as persistence, it has emerged as an attractive molecular target for the design of novel anti-*H. pylori* agents.[7,9] Natural products have historically acted as an invaluable origin of therapeutic leads and persist in contributing substantially to complementary pharmaceutical exploration. Their remarkable structural diversity, biological relevance, and evolutionary optimization enable interactions with a broad spectrum of biological entities that are often difficult to achieve using synthetic compounds alone[10-12]. Analysis of approved drugs revealed that approximately 42% of medicines introduced between 1981 and 2019 originated from natural products, semisynthetic derivatives, or natural product-inspired compounds.[13] This highlights the continuing importance of medicinal plants as sources of novel pharmacologically active molecules. Extensive investigations have demonstrated that numerous medicinal plants and phytoconstituents exhibit significant urease inhibitory activity. Plant-derived metabolites, particularly flavonoids, phenolic compounds, alkaloids, terpenoids, coumarins, and related secondary metabolites, have shown promising inhibitory effects against ureases from different sources, including *H. pylori.*[14-16] Several flavonoids, including quercetin, scutellarin, baicalin, hyperoside, and catechin derivatives, have demonstrated notable anti-urease activity through intermolecular engagements with crucial catalytic entities inside the catalytic pocket of enzyme.[17-19] Furthermore, extracts from numerous medicinal plants, such as *Terminalia chebula*, *Camellia sinensis*, *Pistacia atlantica*, *Smilax glabra*, and *Populus tremula propolis*, have exhibited significant urease inhibitory effects, supporting the potential of plant-derived constituents as valuable sources of novel anti-*H. pylori* agents.[15,19-22] Despite their therapeutic promise, conventional experimental screening of large phytochemical libraries is labor-intensive, time-consuming, and costly. Therefore, there is a pressing need to discover safer and more effective urease inhibitors capable of overcoming the limitations of existing therapeutic agents.[7, 13] In this context, computer-aided drug design (CADD) approaches have surfaced as powerful tools for accelerating lead identification and optimization .[23] Molecular docking enables the prediction of binding affinity and interaction patterns between ligands and target proteins, while *in-silico* absorption, distribution, metabolism, excretion, and toxicity (ADMET) analyses facilitate the early assessment of pharmacokinetic and safety profiles.[24] In addition, molecular dynamics (MD) simulations provide insights into the stability and dynamic behavior of protein-ligand complexes, whereas density functional theory (DFT) calculations contribute to understanding the electronic characteristics and chemical reactivity of lead molecules. The integration of these computational methodologies improves the efficiency of drug discovery and increases the probability of identifying promising therapeutic candidates. Therefore, the present study employed a docking-guided computational strategy to identify potential natural urease inhibitors against *H. pylori*.

MATERIALS AND METHODS

Selection of Natural Compounds

Based on an extensive literature survey, ten medicinal plants reported to possess anti-*H. pylori* activity were selected for the present study (Table 1). Based on the reported phytochemical profiles of these plants, their major bioactive constituents were selected for further investigation (Table 2). The chemical structures of the selected phytoconstituents were retrieved from PubChem

Table 1: Medicinal plants reported for anti-H. pylori activity selected for the present study.

Sr. No.	*Plant name*	*Reference*
1	*Sphaeranthus indicus* (Mundi)	[25]
2	*Tecomaria capensis* (Cape Honeysuckle)	[26]
3	*Chironia baccifera* (Christmas Berry)	[26]
4	*Dodonaea viscosa* (Sand Olive/Aliar)	[27]
5	*Sansevieria yacinthoides* (Piles Root)	[26]
6	*Dombeya rotundifolia* (Wild Pear)	[26]
7	*Cussonia spicata* (Cabbage Tree)	[26]
8	*Setaria megaphylla* (Ribbon Grass)	[26]
9	*Elephantorrhiza elephantina* (Elephant's Root)	[26]
10	*Lippia javanica* (Fever Tea)	[28]

Table 2: Phytoconstituents selected from medicinal plants reported for anti-*H. pylori* activity.

Sr. No.	*Phytoconstituent*	*Structure*
1	Chlorogenic acid	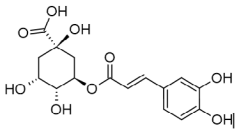
2	Rutin	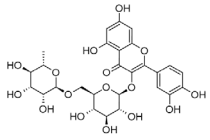
3	Naringenin	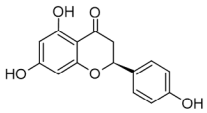
4	3-Hydroxybenzoic acid	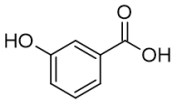
5	Gallic acid	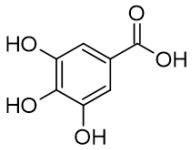
6	Epicatechin	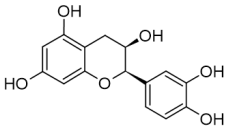
7	3-Hydroxy-4-methoxy benzaldehyde	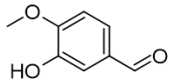
8	Sinapinic acid	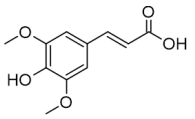
9	Quinic acid	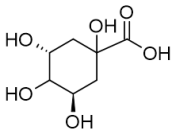
10	2,3′,4,6-Tetrahydroxy-benzophenone	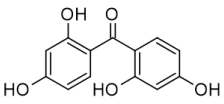
11	2,4,6-Trihydroxybenzoic acid	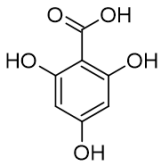
12	3,4-Dihydroxybenzoic acid	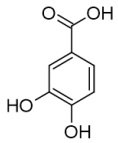
13	Scopolin	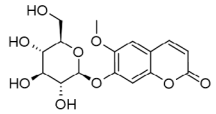
14	Vanilloloside	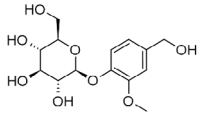
15	7,8-Dihydroxycoumarin	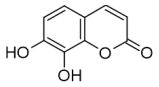
16	Syringin	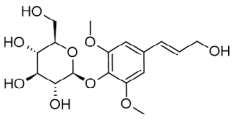
17	3’-(6″-Galloylglucosyl)-phloroacetophenone	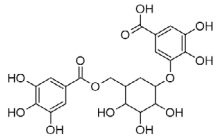
18	4-Coumaroylquinic acid	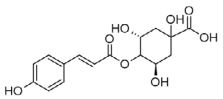
19	Thevetin B	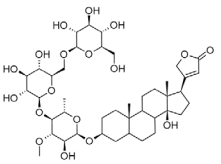
20	Robinetin 3-rutinoside	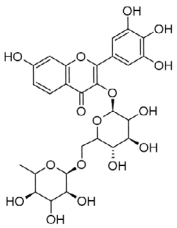
21	Formononetin 7-(6″-methylmalonyl glucoside)	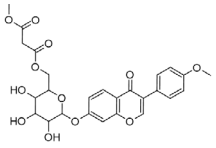
22	Ferulic acid	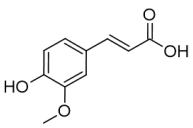

23	Agecorynin C	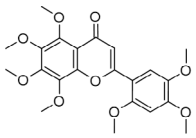	34	2-tert-Butyl-1,4-dimethoxybenzene	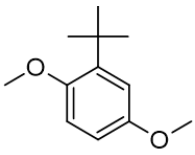
24	Tetracaffeoylquinic acid	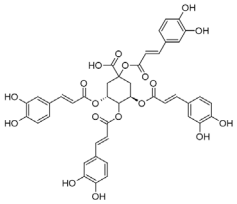	35	9,12-Octadecadienoic acid (Z,Z)	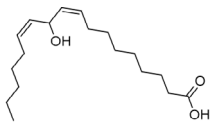
			36	n-Hexadecanoic acid	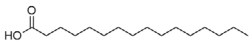
25	5,8,12-Trihydroxy-9-octadecenoic acid	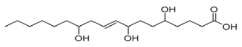	37	n-Tetratetraacontane	$C_{44}H_{90}$
26	Coriandrone D	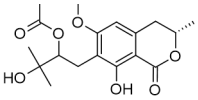	38	α-Pinene	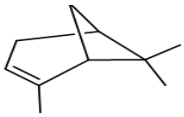
27	9,16-Dihydroxy-palmitic acid	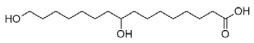			
28	Cinnamodial	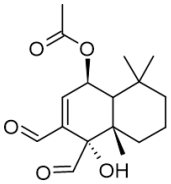	39	Methyl chavicol	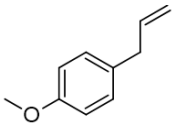
			40	d-Cadinene	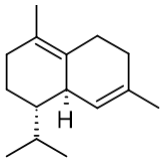
29	Absindiol	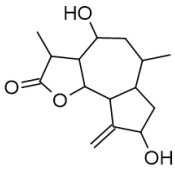			
			41	α-Ionone	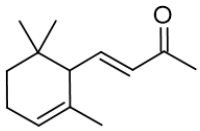
30	Moreollin	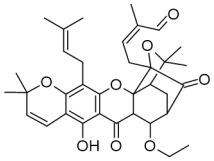			
			42	p-Methoxycinnam-aldehyde	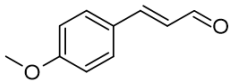
31	Lippioside I	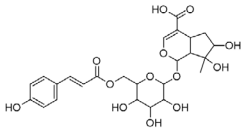	43	α-Terpinene	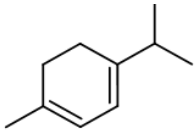
32	Theobromine	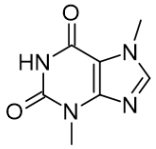	44	Citral	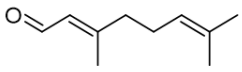
			45	Geraniol	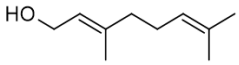
33	10-Acetoxyligustroside	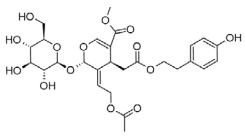	46	Geranyl acetate	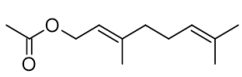

Cant....

47	β-Ionone	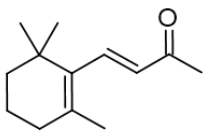
48	Ocimene	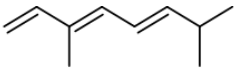
49	Eugenol	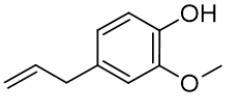
50	Estragole	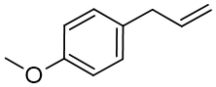
51	Frullanolide	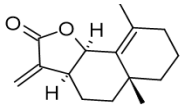
52	4α,8β-Dihydroxyeudesm-7(11)-en-12,8-olide	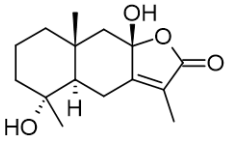
53	2-Hydroxycostic acid	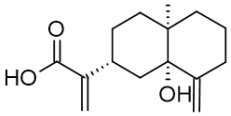
54	β-Eudesmol	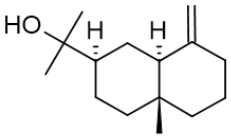
55	Ilicic acid	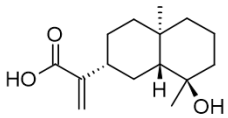
56	Cryptomeridiol	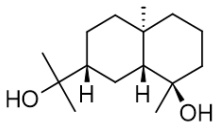
57	4-Epicryptomeridiol	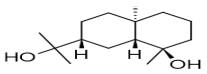
58	Sphaeranthanolide	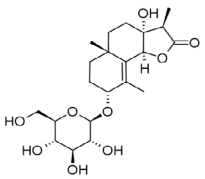
59	Dodonic acid	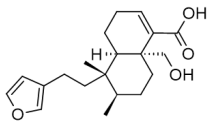
60	Isorhamnetin	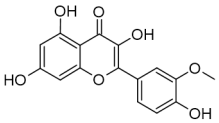
61	5,7,4'-Trihydroxy-3-methoxy-flavone	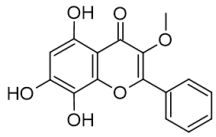
62	6-Hydroxy-3,6,7-trimethoxy-flavone	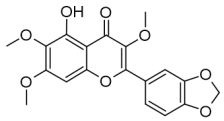
63	5,7-Dihydroxy-flavanone	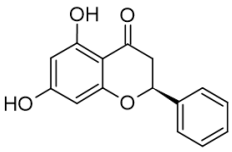
64	5-Hydroxy-7,4'-dimethoxy-flavone	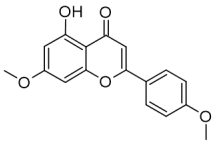
65	(S)-5,4'-Dihydroxy-7-methoxy-flavone	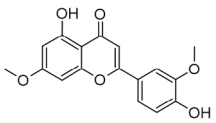
66	3,5,7,4'-Tetra-hydroxyl-3'-methoxy-flavone	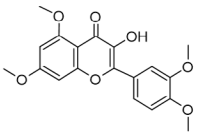
67	Sakuranetin	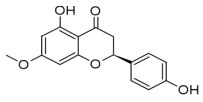
68	Pinocembrin	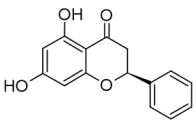
69	Penduletin	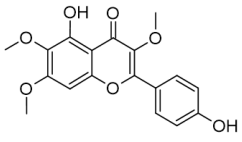

Cant....

70	Viscosol	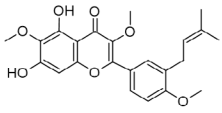
71	Cirsimaritin	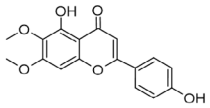
72	Pectolinarigenin	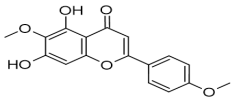
73	Santin	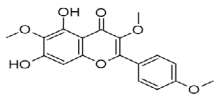
74	Methyl dodovisate A	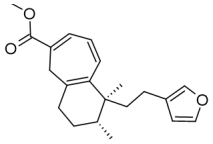
75	Hautriwaic acid	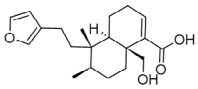
76	Hautriwaic lactone	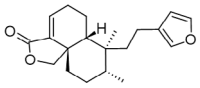
77	(+)-Hardwickiic acid	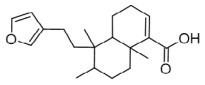
78	Labda-8(17),13-dien-15-olide	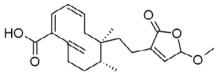
79	Dodonolide	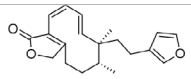
80	Aliarin	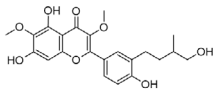
81	Methyl dodonate	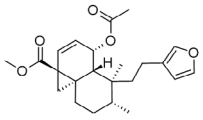
82	Stigmasterol	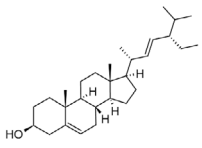
83	Oleanolic acid	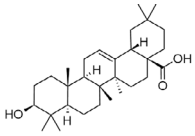
84	(-)-Caryophyllene oxide	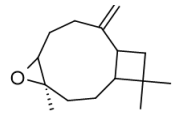
85	11,14,17-Eicosatrienoic acid	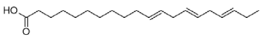
86	Phytol	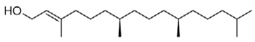
87	Alpha eudesmol	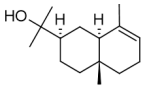
88	Methy dodovisate A	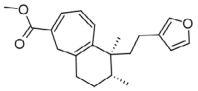
89	Tecomoside	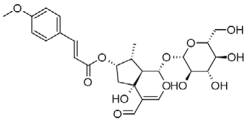
90	Halleridone	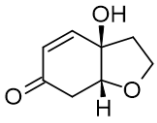
91	Succinic acid decyl-3-oxobut-2-yl ester	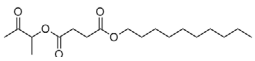
92	Octanoic acid 4-benzyloxyphenyl ester	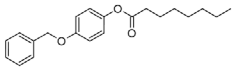
93	Fumaric acid 3,4-dimethoxyphenyl heptyl ester	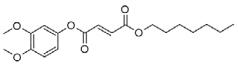
94	Boschniakine	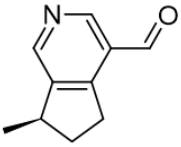
95	Luteolin 7-O-D-glucopyranoside	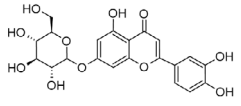
96	Actinidine	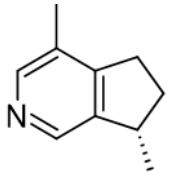

Cant....

97	Skytanthine	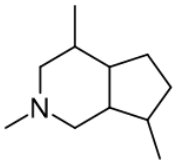
98	Tecomanine	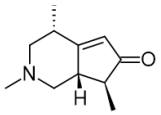
99	Valeric acid pentadecyl ester	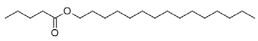
100	Hesperidin	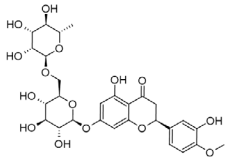
101	Myricetin	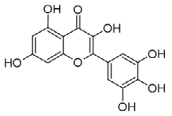
102	Lupeol	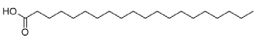
103	Eicosanoic acid	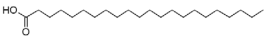
104	Docosanoic acid (behenic acid)	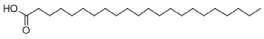
105	Lauric acid	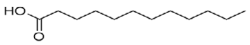
106	Myristic acid	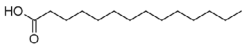
107	Stearic acid	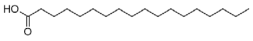
108	Palmitic acid	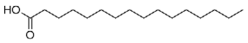
109	Eicosane	
110	Stearyl alcohol	
111	Aristolochic acid I	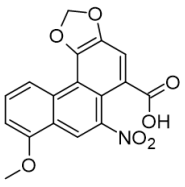
112	Hydrocinnamic acid	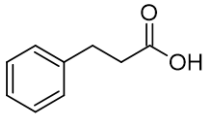
113	Phenethyl alcohol	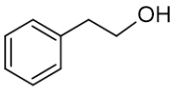
114	Dihydroartemisinin	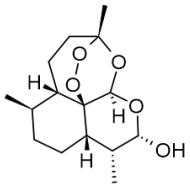
115	(+)-Catechin	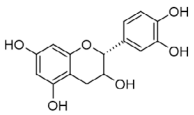
116	Kaempferol	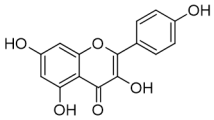
117	Taxifolin	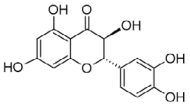
118	Epigallocatechin gallate	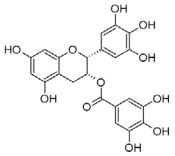
119	Verbascoside	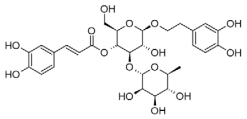
120	Linalool	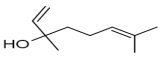
121	Myrcenone	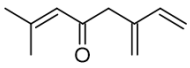
122	Carvone	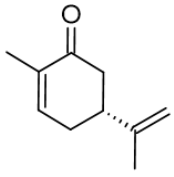
123	Piperitenone	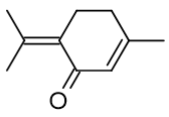
124	Apigenin	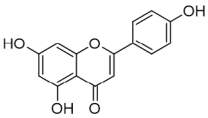

Cant....

125	Luteolin	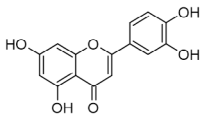
126	Hexadecanoic acid (Palmitic acid)	

and ChemSpider. The final library of phytoconstituents was used for further *in-silico* investigation.

Prediction of Drug Likeness

In the present study, the drug-like attributes of the selected phytoconstituents were evaluated using the SwissADME web server, a widely used online tool for the assessment of physicochemical, pharmacokinetic, and medicinal chemistry properties of small molecules.[29] The canonical SMILES of the selected compounds were obtained from the PubChem database and uploaded to the SwissADME platform. The drug-likeness of the compounds was primarily evaluated according to Lipinski's Rule of Five. The BOILED-Egg accessible within SwissADME was also employed to predict gastrointestinal absorption and blood-brain barrier permeation characteristics.[30] Compounds satisfying the majority of the drug-likeness criteria (Lipinski's Rule of Five) and exhibiting favorable physicochemical properties were considered suitable candidates for further molecular docking studies.

Molecular Docking Studies

Molecular docking studies were carried out to assess the binding affinity and interaction patterns of selected phytoconstituents with *H. pylori* urease using AutoDock Vina.[31] The three-dimensional crystal structure of *H. pylori* urease (PDB ID: 6ZJA) was retrieved from the RCSB Protein Data Bank (PDB) for computational docking studies owing to its high structural quality and biological relevance. This structure represents *H. pylori* urease in complex with a bound inhibitor, providing experimentally validated information regarding the framework of catalytic region, ligand-binding pocket, catalytic residues, and the binuclear nickel center responsible for enzymatic activity. The presence of the co-crystallized ligand facilitates accurate identification of the binding cavity and enables validation of the docking protocol through re-docking studies. Also, 6ZJA provides a high-resolution crystal structure, allowing precise visualization of amino acid residues involved in ligand recognition and enzyme catalysis. The configuration retains the catalytically important nickel ions and active-site residues essential for urease function.[8] The retrieved protein structure was prepared using AutoDock Tools .[32] Co-crystallized ligands, water molecules, and other non-essential heteroatoms were extracted from the protein framework while safeguarding the catalytically vital residues and nickel ions present in the active site. Polar hydrogen atoms were added to the protein, Kollman united atom charges were assigned, and missing atom parameters were corrected wherever necessary. The prepared protein structure was subsequently saved in PDBQT format and used for molecular docking studies. The two-dimensional (2D) chemical structures of the selected compounds were drawn and edited using MarvinSketch (ChemAxon, Budapest, Hungary). The generated structures were saved in MOL2 format and subsequently subjected to three-dimensional (3D) structure generation. The generated 3D ligand structures were visually inspected to ensure correct stereochemistry, bond connectivity, and molecular geometry. Ligand preparation was subsequently performed using AutoDock Tools.[32] Hydrogen atoms were added to satisfy valency requirements and improve the accuracy of molecular interaction calculations. Gasteiger partial atomic charges were assigned to all ligand atoms to facilitate proper electrostatic interaction calculations during docking simulations. Rotatable bonds were identified and defined to allow conformational flexibility of the ligands during the docking process, while maintaining the rigidity of aromatic rings and other structurally constrained regions. Following ligand preparation, all structures were converted into the PDBQT format required by AutoDock Vina. The active site of *H. pylori* urease was identified based on the binding location of the co-crystallized inhibitor present in the crystal structure (PDB ID: 6ZJA) and the reported catalytic residues surrounding the bi-nickel active center. A grid box encompassing the active site region was generated using AutoDock Tools.[32] The grid center coordinates were set at x = 164.176, y = 181.848, and z = 150.637, while the grid dimensions were fixed at 40 × 40 × 40 Å along the x-, y-, and z-axes, respectively. These dimensions were selected to adequately cover the entire active site cavity and accommodate the binding of structurally diverse phytoconstituents. The docking calculations were performed using an exhaustiveness value of 32 in AutoDock Vina to ensure a comprehensive conformational search and improve the reliability of the predicted binding poses. To validate the docking protocol, the co-crystallized ligand was extracted from the crystal structure and re-docked into the urease active site using the same docking parameters. The prepared protein structure and chemical entities in PDBQT format were used as input files for docking simulations. Computational docking calculations were executed within the predefined grid box encompassing the catalytic active site of urease. AutoDock vina used for each ligand and multiple binding conformations (poses) based on the optimization of ligand orientation, position, and torsional flexibility within the active site. The docking algorithm utilizes a gradient-based conformational search strategy combined with an empirical scoring function to estimate the binding free energy of ligand-protein complexes. The docking results

obtained from AutoDock Vina were analyzed based on binding affinity values, binding orientations, and protein-ligand interaction profiles. For each ligand, multiple docking poses were generated, and the conformation exhibiting the lowest binding free energy (kcal/mol) was selected for further analysis. The binding affinity values were used as a preliminary criterion for ranking the compounds, with more negative docking scores indicating stronger predicted interactions and higher binding stability within the urease active site. Detailed interaction analyses were performed to investigate the molecular basis of ligand binding. The selected docked complexes were imported into Discovery Studio (Dassault Systèmes BIOVIA), where various non-covalent interactions between the chemical entities and binding pocket amino acid residues were identified and characterized. Compounds exhibiting strong binding affinity together with favorable interactions involving key catalytic residues were considered promising candidates for further investigation. The interaction patterns of the selected compounds were also compared with those of the reference inhibitor to assess similarities in binding behavior and potential inhibitory mechanisms. The dock complexes pose of three-dimensional visualization was carried out using PyMOL.

Toxicity Prediction Studies

The toxicity profiles of the compounds exhibiting the most favorable docking results were evaluated by use of pkCSM online platform (https://biosig.lab.uq.edu.au/pkcsm/), a widely used computational tool for the prediction of pharmacokinetic and toxicity properties based on graph-based signatures.[33] The pkCSM platform employs predictive models developed from large experimental datasets and provides rapid estimation of various ADMET parameters relevant to drug discovery. The canonical SMILES of the selected compounds were submitted to the pkCSM server, and various toxicity parameters were predicted, including hepatotoxicity, mutagenicity (AMES toxicity), skin sensitization, cardiotoxicity, maximum tolerated dose, acute oral toxicity, and chronic toxicity.

DFT Calculations

DFT calculations were carried out on the compound exhibiting the most favorable docking scores and interaction profiles in order to investigate their electronic properties and chemical reactivity.[34] The 3-D structures of the selected compounds were initially prepared and geometry was optimized using Avogadro (The OpenChemistry). The optimized molecular structures were then subjected to quantum chemical calculations using the ORCA quantum chemistry software package (Frank Neese, FACCTs GmbH, Cologne, Germany). The output files generated by ORCA were subsequently visualized and analyzed using ChemCraft (iSciTech, Inc., Bangalore, India). Geometry optimization was carried out to obtain the lowest-energy stable conformations of the chosen derivatives. Following optimization, frontier molecular orbital (FMO) evaluation was carried out to assess the energy level of the highest occupied molecular orbital (HOMO) and lowest unoccupied molecular orbital (LUMO). The HOMO energy offers insights into the electron-donating ability of a molecule, whereas the LUMO energy signifies its electron-accepting capability. The energy difference between HOMO and LUMO (ΔE) was calculated and used as an indicator of molecular stability, chemical reactivity, and kinetic behavior. In addition, several global reactivity descriptors were calculated using the frontier orbital energies according to Koopmans' theorem. The molecular electrostatic potential surfaces of the selected compounds were also generated to identify electron-rich and electron-deficient regions that may participate in intermolecular interactions with the target protein.

MD Simulations

While molecular docking provides a static representation of protein-ligand interactions, MD simulations offer insights into the time-dependent structural variations, conformational endurance, and intermolecular contacts of the complex in a simulated physiological environment. Desmond (Schrödinger, Inc., New York) was utilized to execute MD simulations for the chosen compounds up to 100 ns.[35] Further, explicit solvent molecules were neutralized by introducing the respective ions and added. The system was relaxed by using the steepest-descent algorithm and minimized the energy through the elimination of any steric clashes or poor contacts between atoms. The equilibrium was developed using a short series with low-temperature and constant-pressure simulations. In this system, positional constraints were applied, followed by the addition of a progressive increase in temperature to make the more stable system and balanced state before the simulation. Further, to achieve adequate outcomes, the simulation was generated for 100 ns and evaluated diverse simulation metrics viz., total system energy, atomic coordinates, root mean square deviation (RMSD) and root mean square fluctuation (RMSF) values, radius of gyration (Rg) and SASA analysis. This facilitated an understanding of the system's dynamic behaviour and provided long-term insights into complex's structure and functional stability.[36]

RESULTS AND DISCUSSION

ADME Prediction

Computational approaches play a crucial role in the initial phases of drug design, specifically in predicting the pharmacokinetic behavior of chemical entities, generally designated as ADME. These techniques rely on theoretically derived statistical and machine learning models that simulate how a compound might behave in the human body, thereby mitigating the requirement

Table 3: ADME properties of the selected natural compounds predicted using the SwissADME web server.
Abbreviations: MW: Molecular weight; LogP: Octanol-water partition coefficient; HBAs: Number of hydrogen bond acceptors; HBDs: Number of hydrogen bond donors; NRBs: Number of rotatable bonds; TPSA: Topological surface area; GI ab.: Gastrointestinal absorption; BBB: Blood-brain barrier permeation; Pgp: Pgp substrate; Lipinski#: No. of violations from Lipinski's Rule of Five.

Ligand	*MW*	*Log P*	*HBAs*	*HBDs*	*NRBs*	*TPSA*	*GI ab.*	*BBB*	*Pgp*	*Lipinski#*
1	354.3	0.57	9	6	5	164.8	Low	No	No	1
2	610.6	2.58	13	8	4	231.5	Low	No	No	3
3	272.3	1.75	5	3	1	87.0	High	No	Yes	0
4	138.1	0.86	3	2	1	57.5	High	Yes	No	0
5	170.1	0.21	5	4	1	98.0	High	No	No	0
6	288.3	1.78	5	4	1	90.2	High	No	Yes	0
7	152.2	1.44	3	1	2	46.5	High	Yes	No	0
8	152.2	1.44	3	1	2	46.5	High	Yes	No	0
9	192.2	0.48	6	5	1	118.2	Low	No	No	0
10	246.2	0.21	5	4	2	98.0	High	No	No	0
11	154.1	0.88	4	3	1	77.8	High	No	No	0
12	154.1	0.66	4	3	1	77.8	High	No	No	0
13	354.3	1.34	9	4	4	138.8	Low	No	No	0
14	316.3	1.58	8	5	5	128.8	Low	No	No	0
15	176.2	1.26	3	2	0	57.5	High	Yes	No	0
16	372.4	1.87	9	5	7	138.1	Low	No	No	0
17	482.4	0.26	13	9	7	234.7	Low	No	No	2
18	338.3	0.76	8	5	5	144.5	Low	No	No	0
19	859.0	2.94	18	9	10	273.0	Low	No	Yes	3
20	610.5	1.89	16	10	6	269.4	Low	No	Yes	3
21	530.5	3.24	12	3	10	171.2	Low	No	Yes	2
22	194.2	1.62	4	2	3	66.8	High	Yes	No	0
23	432.4	4.20	9	0	8	94.8	High	No	No	0
24	840.7	2.18	18	9	17	304.3	Low	No	Yes	3
25	330.5	2.61	5	4	15	98.0	High	No	Yes	0
26	352.4	2.85	7	2	6	102.3	High	No	No	0
27	288.4	3.23	4	3	15	77.8	High	Yes	Yes	0
28	308.4	1.79	5	1	4	80.7	High	No	No	0
29	266.3	1.67	4	2	0	66.8	High	Yes	Yes	0
30	590.7	4.79	8	1	7	108.4	Low	No	Yes	1
31	538.5	0.65	13	7	8	212.7	Low	No	No	3
32	180.2	1.22	3	1	0	72.7	High	No	No	0
33	582.6	3.10	14	5	14	207.7	Low	No	No	2
34	194.3	2.95	2	0	3	18.5	High	Yes	No	0
35	296.4	2.95	3	2	14	57.5	High	Yes	No	0
36	256.4	3.85	2	1	14	37.3	High	Yes	No	1
37	619.2	11.31	0	0	41	0.0	Low	No	Yes	2

Cant....

38	136.2	2.63	0	0	0	0.0	Low	Yes	No	1
39	148.2	2.47	1	0	3	9.2	High	Yes	No	0
40	204.4	3.41	0	0	1	0.0	Low	No	No	1
41	192.3	2.81	1	0	2	17.1	High	Yes	No	0
42	162.2	1.96	2	0	3	26.3	High	Yes	No	0
43	136.2	2.70	0	0	1	0.0	Low	Yes	No	0
44	152.2	2.51	1	0	4	17.1	High	Yes	No	0
45	154.3	2.52	1	1	4	20.2	High	Yes	No	0
46	196.3	3.27	2	0	6	26.3	High	Yes	No	0
47	192.3	2.77	1	0	2	17.1	High	Yes	No	0
48	136.2	2.94	0	0	3	0.0	Low	Yes	No	0
49	164.2	2.37	2	1	3	29.5	High	Yes	No	0
50	148.2	2.47	1	0	3	9.2	High	Yes	No	0
51	232.3	2.76	2	0	0	26.3	High	Yes	No	0
52	266.3	2.30	4	2	0	66.8	High	Yes	Yes	0
53	250.3	2.28	3	2	2	57.5	High	Yes	No	0
54	222.4	3.06	1	1	1	20.2	High	Yes	No	0
55	252.4	2.31	3	2	2	57.5	High	Yes	No	0
56	240.4	2.89	2	2	1	40.5	High	Yes	No	0
57	240.4	2.83	2	2	1	40.5	High	Yes	No	0
58	428.5	2.14	9	5	3	145.9	Low	No	Yes	0
59	332.4	2.73	4	2	5	70.7	High	Yes	Yes	0
60	316.3	2.35	7	4	2	120.4	High	No	No	0
61	300.3	1.81	6	3	2	100.1	High	No	No	0
62	372.3	3.56	8	1	4	96.6	High	No	No	0
63	256.3	2.11	4	2	1	66.8	High	Yes	No	0
64	298.3	2.55	5	1	3	68.9	High	Yes	No	0
65	314.3	3.15	6	2	3	89.1	High	No	No	0
66	358.3	3.41	7	1	5	87.4	High	No	No	0
67	286.3	2.41	5	2	2	76.0	High	Yes	No	0
68	256.3	2.11	4	2	1	66.8	High	Yes	No	0
69	344.3	2.84	7	2	4	98.4	High	No	No	0
70	412.4	4.04	7	2	6	98.4	High	No	No	0
71	314.3	2.56	6	2	3	89.1	High	No	No	0
72	314.3	2.58	6	2	3	89.1	High	No	No	0
73	344.3	3.25	7	2	4	98.4	High	No	No	0
74	326.4	3.79	3	0	5	39.4	High	Yes	No	0
75	332.4	2.30	4	2	5	70.7	High	Yes	Yes	0
76	314.4	3.18	3	0	3	39.4	High	Yes	No	0
77	316.4	3.04	3	1	4	50.4	High	Yes	No	0
78	360.4	3.04	5	1	5	72.8	High	Yes	No	0

Cant....

79	312.4	3.04	3	0	3	39.4	High	Yes	No	0
80	416.4	3.05	8	4	7	129.6	High	No	No	0
81	386.5	3.54	5	0	7	65.7	High	Yes	No	0
82	412.7	5.08	1	1	5	20.2	Low	No	No	1
83	456.7	3.94	3	2	1	57.5	Low	No	No	1
84	220.4	3.15	1	0	0	12.5	High	Yes	No	0
85	306.5	4.50	2	1	15	37.3	High	No	No	1
86	296.5	4.85	1	1	13	20.2	Low	No	Yes	1
87	222.4	3.12	1	1	1	20.2	High	Yes	No	0
88	326.4	3.79	3	0	5	39.4	High	Yes	No	0
89	536.5	2.76	12	5	9	181.4	Low	No	Yes	2
90	154.2	1.25	3	1	0	46.5	High	No	No	0
91	328.4	3.71	5	0	16	69.7	High	Yes	No	0
92	326.4	4.03	3	0	11	35.5	High	Yes	No	1
93	350.4	4.22	6	0	13	71.1	High	Yes	No	0
94	161.2	1.67	2	0	1	30.0	High	Yes	No	0
95	448.4	1.76	11	7	4	190.3	Low	No	Yes	2
96	147.2	2.13	1	0	0	12.9	High	Yes	No	0
97	167.3	2.80	1	0	0	3.2	Low	Yes	No	0
98	179.3	2.31	2	0	0	20.3	High	Yes	No	0
99	312.5	5.48	2	0	18	26.3	Low	No	No	1
100	610.6	0.89	15	8	7	234.3	Low	No	Yes	3
101	318.2	1.08	8	6	1	151.6	Low	No	No	1
102	426.7	4.72	1	1	1	20.2	Low	No	No	1
103	312.5	4.56	2	1	18	37.3	Low	No	No	1
104	340.6	5.26	2	1	20	37.3	Low	No	No	1
105	200.3	2.70	2	1	10	37.3	High	Yes	No	0
106	228.4	3.32	2	1	12	37.3	High	Yes	No	0
107	284.5	4.30	2	1	16	37.3	High	No	No	1
108	256.4	3.85	2	1	14	37.3	High	Yes	No	1
109	282.6	5.64	0	0	17	0.0	Low	No	No	1
110	270.5	4.86	1	1	16	20.2	High	No	No	1
111	341.3	1.96	7	1	3	110.8	High	No	No	0
112	150.2	1.50	2	1	3	37.3	High	Yes	No	0
113	122.2	1.70	1	1	2	20.2	High	Yes	No	0
114	284.4	2.49	5	1	0	57.2	High	Yes	No	0
115	290.3	1.47	6	5	1	110.4	High	No	Yes	0
116	286.2	1.70	6	4	1	111.1	High	No	No	0
117	304.3	1.08	7	5	1	127.5	High	No	No	0
118	458.4	1.53	11	8	4	197.4	Low	No	No	2
119	624.6	2.15	15	9	11	245.3	Low	No	Yes	3

Cant....

120	154.3	2.70	1	1	4	20.2	High	Yes	No	0
121	150.2	2.32	1	0	4	17.1	High	Yes	No	0
122	150.2	2.27	1	0	1	17.1	High	Yes	No	0
123	150.2	2.31	1	0	0	17.1	High	Yes	No	0
124	270.2	1.89	5	3	1	90.9	High	No	No	0
125	286.2	1.86	6	4	1	111.1	High	No	No	0
126	256.4	3.85	2	1	14	37.3	High	Yes	No	1

for widespread laboratory and animal-based assays during preliminary stages.[37-39] SwissADME estimates crucial descriptors including molecular weight (MW), gastrointestinal (GI) absorption, blood-brain barrier (BBB) permeability, P-glycoprotein (P-gp) substrate assessment, cytochrome P450 (CYP450) enzyme inhibition, and skin penetration coefficient (Log Kp), among others. Based on Lipinski's rule of five guidelines, a molecule is more expected to show adequate oral bioavailability if it satisfies the following criteria: Molecular Weight ≤ 500 Da; LogP (octanol-water partition coefficient) ≤ 5; number of hydrogen bond donors (HBDs) ≤ 5; number of hydrogen bond acceptors (HBAs) ≤ 10. Chemical entities that comply with these parameters are typically expected to possess favorable ADME behaviors and present a higher probability to excel as orally bioavailable therapeutic leads.[29,38] A total of 126 phytoconstituents were subjected to SwissADME prediction to assess their drug-likeness and pharmacokinetic suitability. Out of these, 92 compounds fulfilled the selected drug-likeness criteria, whereas 34 compounds exhibited one or more unfavorable physicochemical characteristics that may limit their oral bioavailability and drug development potential (Table 3). The finding that nearly three-fourths of the screened compounds possess favorable drug-like properties indicates that the phytochemical selection contains a substantial number of molecules with characteristics comparable to orally active therapeutic agents.

The majority of compounds classified as drug-like possessed MW ranging between 120 and 450 Da, which is considered optimal for oral drug candidates. These compounds are expected to diffuse more readily across biological membranes. Conversely, several glycosylated flavonoids and polyphenolic compounds such as rutin (610.6 Da), hesperidin (610.6 Da), verbascoside (624.6 Da), thevetin B (859.0 Da), and tetracaffeoylquinic acid (840.7 Da) exceeded the recommended MW threshold, contributing to poor oral absorption and multiple Lipinski violations. Lipophilicity is a critical determinant of membrane permeability and bioavailability. Most drug-like phytoconstituents exhibited LogP values between 1 and 5, indicating a favorable balance between aqueous solubility and membrane penetration. However, highly hydrophobic compounds such as n-tetratetracontane (LogP 11.31), eicosane (5.64), valeric acid pentadecyl ester (5.48), and docosanoic acid (5.26) showed excessive lipophilicity, which may adversely affect aqueous solubility and systemic bioavailability. Drug-like compounds generally possessed HBD and HBA counts within Lipinski limits (HBD ≤ 5 and HBA ≤ 10). Flavonoids such as apigenin, luteolin, pinocembrin, and sakuranetin demonstrated balanced hydrogen bonding capabilities that favor receptor interactions while maintaining membrane permeability. In contrast, highly glycosylated compounds such as rutin, hesperidin, verbascoside, luteolin-7-O-glucoside, and robinetin-3-rutinoside exhibited very high HBA and HBD values, resulting in increased polarity and reduced passive diffusion across intestinal membranes. TPSA values below approximately 140 $Å^2$ are generally associated with favorable oral absorption. Most of the 92 drug-like compounds exhibited TPSA values within this desirable range. SwissADME predicted high GI absorption for the majority of drug-like molecules. Notable examples include naringenin, ferulic acid, eugenol, geraniol, citral, pinocembrin, sakuranetin, kaempferol, apigenin, luteolin, and dihydroartemisinin. These compounds are therefore more likely to achieve therapeutically relevant plasma concentrations following oral administration. Compounds predicted to have low GI absorption were predominantly large polyphenols, glycosides, and highly polar constituents such as rutin, chlorogenic acid, hesperidin, verbascoside, tecomoside, and luteolin-7-O-glucoside. Their poor absorption can be attributed to elevated molecular weight and TPSA values. Only a limited number of compounds were predicted to cross the BBB. Examples include 3-hydroxybenzoic acid, ferulic acid, α-ionone, β-eudesmol, α-eudesmol, geraniol, linalool, methyl chavicol, and several terpenoids. These compounds may possess potential for neurological or central nervous system applications. Most flavonoids, phenolic acids, and glycosides were predicted to be BBB-impermeable because of their higher polarity and larger molecular size. As shown in (Figure 1), the majority of the compounds were distributed within the white region, suggesting a high probability of passive HIA. Several compounds were also located within the yellow yolk, indicating their potential ability to cross the BBB.P-

Table 4: Docking score and residues involved in binding interactions of the selected compounds with H. pylori urease.

Ligand	*ΔG (kcal/mol)*	*Hydrogen Bond Interactions (Bond Distance)*	*Hydrophobic and Other Interactions (Residues Involved)*
3	-7.1	Arg338 (2.98 Å), Ala278 (2.90 Å), Asp362 (2.96, 3.08 Å), His138 (3.10 Å)	Cys321 (Pi-Donor), His221 (Pi-Pi T Shaped), Met366 (Pi-Alkyl), Ala365(Pi-Alkyl), Cys321 (Pi-Sulfer)
4	-5.2	Asn168 (2.89 Å), His221 (2.92 Å), His248 (3.18 Å), Ala169 (3.34 Å), Asp362 (2.97 Å), His138 (3.20 Å), Ala365 (3.30 Å)	Asp362 (Pi-Anion), Ala365 (Pi-Alkyl)
5	-5.2	Ala365 (2.83 Å), Asp362 (2.86 Å), Ala169 (2.73 Å), His221 (2.89 Å), Arg338 (3.11 Å), Ala278 (2.94 Å)	Met366 (Pi-Sulfur)
6	-7.4	Ala169 (2.91 Å), Glu222 (2.92 Å)	His248 (Pi-Pi Stacked), Met317 (Amide-Pi Stacked), Leu318, His314, Leu318 (Pi-Alkyl), Leu318, Met317, Met366, Cys321 (Alkyl), Met317, Met366 (Pi-Sulfur)
7	-4.6	Arg338 (2.98, 3.16 Å), Ala278 (2.82, 3.15 Å)	Leu318, Cys321, Met317 (Pi-Alkyl), Met366 (Pi-Sulfur)
8	-5.9	Asp362 (2.77 Å), His138 (3.09 Å), Ala365 (3.24 Å), Arg338 (3.16 Å), His332 (2.18 Å)	His322 (Pi-Alkyl), Met366 (Pi-Sulfur),
9	-5.3	Ala169 (2.90 Å), Gly279 (2.75, 3.05 Å), Asp362 (3.30 Å), Asp223 (3.15 Å)	His221 (C-H Bond)
10	-6.3	Ala169 (2.84 Å), Cys321 (3.64 Å), Arg338 (3.10 Å), Ala278 (2.87 Å), Gly279 (2.77 Å)	His248 (C-H Bond), Cys321 (Pi-Donor Bond), Cys321 (Pi-Sulfur)
11	-4.9	Ala169 (2.82 Å), His248 (3.15 Å), Asp362 (2.75 Å), Ala169 (2.82 Å), Asp362 (3.55 Å)	Met366 (Pi-Sulfur)
12	-4.9	His138 (3.18 Å), Ala365 (3.17 Å), Asp362 (2.83,3.14 Å), His248 (3.25 Å)	Met366 (Pi-Sulfur)
13	-7.4	Ala169 (2.81 Å), His221 (3.04 Å), Glu222 (3.05 Å), His322 (3.00 Å)	Cys321 (Pi Donor Hydrogen Bond), Met317 (Amide Pi-Stacked), Cys321 (Alkyl), Leu318, Met366, Cys321 (Pi-Alkyl), Met317, Met366, Cys321 (Pi-Sulfur)
14	-6.6	Ala278 (2.74 Å), Ala365 (2.81 Å), Ala362 (3.14 Å), Ala169 (2.90, 3.14 Å), Asp223 (3.06 Å), His322 (3.29 Å)	His314, Ala169, Met317 (C-H Bond), Met317 (Amide-Pi Stacked), Cys321 (Pi-Donor Hydrogen Bond), Cys321 (Alkyl), Leu318 (Pi-Alkyl), Met366 (Pi-Sulfur)
15	-5.7	Ala169 (2.95 Å), His221 (3.10 Å), Ala365 (3.16 Å), Asp362 (3.22, 3.00 Å)	Met366 (Pi-Sulfur)
16	-5.9	Asp223 (2.94 Å), Glu222 (3.07, 2.95 Å), Thr251 (3.03 Å), Met366 (3.16 Å)	Cys321(Pi-Alkyl), Met366 (Pi-Alkyl), His322 (Unfavourable Acceptor-Acceptor), Gly280 (C-H Bond), Ala365, Cys321, Leu318, Met366 (Alkyl)
18	-7.0	Asn168 (2.88 Å), Ala169 (2.87 Å), His221 (3.02 Å), Asp362 (2.92 Å), Gly279 (2.94 Å), His314 (2.76 Å)	Met317 (Amide-Pi Stacked), His221, Cys321, Leu318 (Pi-Alkyl), Met366 (Pi-Sulfur), Ala365 (Alkyl)
22	-5.5	His322 (3.03, 3.50 Å), His138 (3.05 Å), Asp362 (2.83, 3.10 Å), His248 (3.00 Å)	Cys321, Leu318 (Alkyl), His322 (Pi-Donor Bond), His322, Ala169 (Pi-Alkyl)
23	-6.3	Met366 (4.47, 3.12, 4.78 Å)	Gly279, Asp223, Glu222 (C-H Bond), Asp223 (Pi-Anion), Met366, Met317, Cys321, Leu252 (Alkyl), His248, His322 (Pi-Alkyl), Cys321 (Pi-Sulfur)
25	-4.7	Asn168 (2.97 Å), Ala169 (2.93, 3.55 Å), His221 (2.81 Å), His322 (3.15, 4.11 Å), Arg338 (3.24 Å)	Ala169 (C-H Bond), His322 (Pi-Donor Hydrogen Bond), Cys321, Met366, Leu318 (Alkyl), His322 (Pi-Alkyl)
26	-6.9	Arg338 (2.80, 2.91 Å), Cys321 (3.47 Å)	Gly279, Asp362 (C-H Bond), Cys321, Met317, Met366 (Alkyl), His248, His322 (Pi-Alkyl)
27	-4.1	His314 (3.22 Å), His248 (2.93 Å), His221 (3.15 Å)	His322, His248 (Pi-Alkyl), Ala169, Asp362, His138 (C-H Bond), Cys321, Met366, Ala169, Ala365 (Alkyl)
28	-5.7	-	Asn168 (C-H Bond), Leu318, Cys321, Met366 (Alkyl), His322 (Pi-Alkyl)

Cant....

29	-6.3	Arg338 (2.83 Å), Gly279 (3.06 Å)	His248 (Pi Alkyl), Cys321, Met366, Met317 (Alkyl)
32	-5.2	-	Leu318, Cys321, Ala365 (Alkyl), His138, His322 (Pi-Alkyl), Asp362, Ala365 (C-H Bond), Met366 (Pi-Sulfur)
34	-5.1	-	Asp362, His274, Ala278 (C-H Bond), Met366 (Pi-Sulfur), Met366 (Alkyl), His138, His136, His248, His221, His274 (Pi-Alkyl)
35	-4.9	Gly279 (2.99 Å), His322 (3.19 Å)	His248 (C-H Bond), Ala169, Leu318, Met366, Met317, Cys321 (Alkyl)
39	-4.4	-	Asp362, His138, His136, His274 (C-H Bond), Met366 (Pi-Sulfur), Met366 (Alkyl), His138, His221, His136, His248, His274 (Pi-Alkyl)
41	-5.1	-	Ala169, Met366, Cys321 (Alkyl), His221, His322 (Pi-Alkyl)
42	-4.7	His248 (3.02 Å)	Ala169, Ala365 (Pi-Alkyl), Ala169 (Alkyl), Asp362, Asn168 (C-H Bond)
43	-4.5	-	Leu318, Ile339, Cys321, Met366 (Alkyl), Cys321, Met366 (Pi-Sulfur), Leu318, Met317 (Pi-Alkyl)
44	-4.3	His248 (3.06 Å)	Ala169, Ala365, Met366 (Alkyl), His221, His248 (Pi-Alkyl)
45	-4.5	His136 (2.94 Å), His138 (3.01 Å), Asp362 (3.00 Å)	Ala365, Cys321, Met366 (Alkyl), His221, His248 (Pi-Alkyl)
46	-5.2	His248 (2.92 Å)	His248 (C-H Bond), Met366, Met317, Leu318, Ile339, Cys321 (Alkyl), His248 (Pi-Alkyl)
47	-5.1	Arg338 (3.25 Å)	Met366 (Alkyl), His322 (Pi-Alkyl)
48	-4.2	-	His322 (Pi-Alkyl), Leu318, Met317, Met366, Leu318, Ile339, Cys321 (Alkyl)
49	-4.9	Asp362 (2.71 Å), Ala365 (3.04 Å)	His248, His221, His136, His274, His138 (Pi-Alkyl), Asp362, His138, His136 (C-H Bond)
50	-4.3	-	His138, Asp362, His274, His136 (C-H Bond), Met366, Cys321 (Alkyl), His138, His221, His248, His274, His136 (Pi-Alkyl)
51	-6.0	Arg338 (3.06 Å)	Leu318, Met366, Cys321 (Alkyl), His248, His322 (Pi-Alkyl), Gly280 (C-H Bond)
52	-6.7	Arg388 (3.23 Å), Ala278 (3.30 Å)	Ala169, Cys321, Met366, Met317 (Alkyl), His248, His322 (Pi-Alkyl)
53	-6.2	Asp223 (2.85 Å), Asp362 (2.88 Å), His138 (3.21 Å), Ala365 (3.19 Å)	His221 (C-H Bond), His248, His322 (Pi Alkyl), Ala169 (Alkyl)
54	-5.9	Gly279 (2.93 Å), Arg338 (3.22 Å)	Cys321, Met366, Met317, Leu318 (Alkyl), His248, His322, His221 (Pi-Alkyl), Gly280 (C-H Bond)
55	-6.8	His248 (2.87 Å), Asp362 (2.70 Å), His138 (2.96 Å), His136 (3.24 Å), Glu222 (2.94 Å)	Cys321, Ala169 (Alkyl), His322, His221 (Pi-Alkyl)
56	-5.7	His221 (3.15 Å), Ala169 (2.93 Å), Asp223 (2.96 Å)	Cys321, Met366, Ala365, Ala169 (Alkyl), His322 (Pi-Sigma)
57	-5.9	His322 (3.31 Å), Asp362 (3.13 Å), Asp365 (2.70 Å)	Cys321, Met366, Ala169 (Alkyl), His322, His221, His274, His248 (Pi-Alkyl)
58	-7.6	Gly279 (2.71, 2.91 Å), Ala169 (2.97, 3.05 Å), Asn168 (3.02 Å), Asp165 (2.70 Å)	Cys321, Ala169 (Alkyl), His322 (Pi-Alkyl)
59	-7.0	Asp362 (3.05, 2.96 Å), His138 (3.24 Å), Ala365 (2.79,3.27 Å), Leu318 (3.23 Å)	Ala365, Cys321 (Alkyl), His221, His248, His322, Met317, Cys321 (Pi-Alkyl), Leu318 (Pi-Sigma)
60	-7.1	Asn168 (3.00 Å), Asp362 (317 Å)	His248 (C-H Bond), His322 (Pi-Donor Hydrogen Bond), Glu222, Asp223 (Pi-Anion), Ala365, His322 (Pi-Alkyl), His322 (Pi-Pi T Shaped)

Cant....

61	-7.2	Asp362 (2.96, 2.59 Å), Ala365 (2.70 Å), Cys321 (3.69 Å)	Arg338 (Pi Cation), Met317, Cys321, Leu318 (Pi-Alkyl), His322 (C-H Bond), Met366 (Pi-Sulfur)
62	-6.4	Met366 (3.11 Å), Arg338 (2.99 Å)	Met317, Cys321, His221, His248 (Pi-Alkyl), His322 (Pi-Pi T Shaped), Met317 (Pi-Sigma), Glu222, Asp223 (C-H Bond), Cys321 (Pi-Donor Bond), Cys321 (Pi-Sulfur)
63	-6.3	Ala278 (2.91 Å), Arg338 (3.04 Å)	Cys321 (Pi-Donor Bond), His221 (Pi-Pi T Shaped), Gly279 (Amide-Pi T Shaped), Met366, Ala365 (Pi-Alkyl)
64	-7.0	Ala365 (3.21 Å)	His314 (C-H Bond), Glu222 (Pi-Anion), Arg338 (Pi-Cation), His322 (Pi-Pi T Shaped), Leu252, Met366, Met317, Leu318 (Alkyl), Met366, Cys321 (Pi-Alkyl)
65	-7.2	Asn168 (2.93 Å)	His221, His248 (C-H Bond), Glu222, Asp223 (Pi-Anion), His322 (Pi-Pi T Shaped), His322, His248, His274, His136, His138, His221, Ala169, Ala365 (Pi-Alkyl)
66	-6.8	Asp223 (3.04 Å)	Asp362, Gly279, His221 (C-H Bond), Arg338 (Pi Cation), Asp223 (Pi-Anion), Met317, Cys321, Met366, Leu252 (Alkyl), Cys321, His322 (Pi-Alkyl)
67	-7.3	His138 (3.12 Å), Asp362 (3.06 Å), Arg338 (3.25 Å)	Cys321 (Pi-Donor Hydrogen Bond), His221 (Pi-Pi T Shaped), Met366, Leu318 (Alkyl), Met365, Ala365 (Pi Alkyl), Cys321 (Pi-Sulfur)
68	-6.3	Met366 (3.62 Å), Arg338 (3.02 Å), Ala365 (3.02 Å), Asp362 (3.13 Å)	His221 (C-H Bond), Ala365, Cys321, Ala169 (Pi-Alkyl), His248, His322 (Pi-Pi T Shaped), Met366 (Pi-Sulfur)
69	-5.9	Asp223 (2.80 Å)	Gly279 (C-H Bond), Cys321, Ala365 (Pi-Alkyl), Asp223 (Pi-Anion)
70	-7.0	Asp223 (2.92 Å), Arg338 (3.03 Å), Gly279 (3.03 Å)	Glu222 (C-H Bond), Cys321 (Pi-Sulfur), Met317 (Pi Sigma), His248, His322, Met366 (Pi Alkyl), Met317, Val320 (Alkyl)
71	-6.4	Asn168 (2.85 Å), Cys321 (3.51 Å), His314 (3.15 Å)	Met366, Met317 (Pi-Sulfur), Ala169, Cys321, Leu318 (Pi-Alkyl)
72	-6.5	Arg338 (2.82 Å), Glu222 (2.27 Å), Asp223 (3.19 Å), Met366 (3.64 Å)	Ala365, Cys321, His322 (Pi-Alkyl), His322 (Pi-Pi T Shaped), Gln364 (C-H Bond)
73	-6.2	Arg338 (2.97 Å), Gly279 (3.03 Å), Asp223 (2.96 Å)	Glu222 (C-H Bond), Met317 (Alkyl), Met317 (Pi-Sigma), Cys321 (Pi-Sulfur), Cys321 (Pi-Donor Bond), Met366, His248, His322 (Pi-Alkyl)
74	-6.8	-	Ile339, Leu318, Met366, Ala169 (Alkyl), His221 (Pi-Pi T Shaped), Asp362 (Pi-Anion), Cys321 (Pi-Donor Bond), Met366, His322, Ala365 (Pi-Alkyl), Cys321 (Pi-Sulfur), His314 (C-H Bond)
75	-6.3	Met366 (3.34 Å)	Cys321, Met366 (Alkyl), His322 (Pi-Pi T Shaped), Glu222 (Pi-Anion)
76	-7.0	His248 (3.23 Å)	Leu318, Cys321 (Pi-Alkyl), Ala365, Cys321, Met366 (Alkyl), Met366, Met317(Pi-Sulfur), Ala278 (C-H Bond)
77	-7.4	Asp362 (3.03 Å), Gly279 (3.00 Å)	His314 (C-H Bond), His322, Cys321, Leu318 (Pi-Alkyl), Met317, Met366 (Pi-Sulfur), Cys321, Ala365 (Alkyl)
78	-7.2	Asp362 (3.01 Å), Ala365 (3.16 Å), His138 (3.36 Å)	Ala169, Cys321 (Alkyl), His322 (C-H Bond)
79	-6.3	-	His221 (Pi-Pi T Shaped), Ala365, His322 (Pi-Alkyl), His136, Ala278 (C-H Bond), Met366, Cys321 (Alkyl)
80	-6.8	Leu318 (3.18 Å), His314 (2.81 Å), Gly279 (3.04 Å), Arg338 (2.97 Å), Gln364 (2.80 Å)	Ala365 (Pi Alkyl), Gly280, Ala365 (C-H Bond), Cys321, Met317 (Alkyl)
81	-6.4	Cys321 (3.14 Å)	Met366, Ile339, Leu318, Cys321, Ala365 (Alkyl), Ala169 (Pi-Sigma), Asp165, His314 (C-H Bond)

Cant....

84	-5.5	-	Cys321, Ala365, Met366, Ala169 (Alkyl), His138, His248, His274, His221 (Pi-Alkyl)
87	-5.8	Arg338 (3.15 Å), Gly279 (2.82 Å)	His248 (C-H Bond), Leu318, Met366, Met317, Cys321 (Alkyl), His322, His221, His248 (Pi-Alkyl)
88	-7.1	His248 (2.71 Å), Met366 (3.07 Å),	His221, His248, His274, His322, Phe273 (Pi-Alkyl), Ala169, Cys321 (Alkyl), His136 (C-H Bond), Met366 (Pi-Sulfur)
90	-4.7	Ala365 (2.99 Å), Asp362 (3.21 Å)	His221, His248, His138 (Pi-Alkyl), Ala365 (Alkyl)
91	-4.8	Arg338 (3.02 Å)	Ala169, Met366, Cys321, Ala365 (Alkyl), Ala169 (C-H Bond)
93	-5.4	Met366 (3.16 Å)	His322, Ala365, Ala169, His136, His221, His138, His248 (Pi-Alkyl), Cys321, Met317, Met366 (Alkyl) Asp362, His274, Met317 (C-H Bond)
94	-4.8	His248 (3.16 Å),	Asp362, Ala365 (C-H Bond), His322, His221(Pi-Alkyl), Met366 (Pi-Sulfur), Ala169 (Alkyl),
96	-4.5	Arg338 (3.14 Å)	Met366 (Alkyl), His248, His221 (Pi-Alkyl)
97	-4.5	-	His221, His322, His248 (Pi-Alkyl), Cys321, Met366 (Alkyl), His221, Ala169, (C-H Bond)
98	-5.1	Arg338 (3.08 Å)	Met317 (C-H Bond), Cys321, Met366, Met317, Leu318 (Alkyl), His322 (Pi-Alkyl)
105	-4.2	His248 (2.93 Å), Asp362 (3.10 Å), Gly279 (2.80 Å)	Ala365, Cys321, Leu318, Met317 (Alkyl)
106	-4.3	His138 (3.33 Å), Ala365 (3.21 Å), Asp362 (3.02 Å), His248 (3.21 Å)	His322, His221, His248 (Pi-Alkyl), Met366, Cys321 (Alkyl)
111	-6.9	Ala278 (2.74 Å), Arg338 (2.99, 2.93, 2.98 Å)	His322 (Pi-Pi T Shaped), His322 (Unfavourable Acceptor-Acceptor), Cys321 (Pi-Donor Hydrogen Bond), Met366, Cys321, Ala169 (Pi-Alkyl)
112	-5.0	Asp362 (2.86 Å), His138 (2.93 Å), His136 (2.85 Å), His248 (2.87 Å)	His221, His248 (Pi-Pi T Shaped), Ala169, (Pi Alkyl)
113	-4.3	Asp362 (3.08 Å), His138 (3.12 Å), His 136 (2.98 Å)	Met366 (Pi-Sulfur)
114	-6.5	Ala365 (2.98 Å)	Ala365, Cys321, Leu318, Met366 (Alkyl), His248 (C-H Bond), His322, His221, His248 (Pi-Alkyl)
115	-7.5	Ala169 (2.84 Å), His221 (2.91 Å), Asp223 (2.90 Å), Ala278 (2.70 Å), His314 (2.62 Å), Arg338 (3.76, 3.17 Å), His322 (3.20 Å)	Cys321, His322, Leu318, Ala169 (Pi-Alkyl), Cys321(Alkyl), Met317, Met366 (Pi-Sulfur)
116	-7.0	His136 (3.38 Å), Asp362 (2.77 Å), Ala169 (2.71 Å), Cys321 (3.48 Å), Leu318 (3.09 Å), His314 (2.41 Å)	Cys321, Met317, Leu318 (Pi-Alkyl), His248 (Pi-Pi T Shaped), Met366 (Pi-Sulfur)
117	-7.1	Ala365 (3.07 Å), Ala169 (2.70 Å), Asp223 (3.08 Å), Glu222 (3.32 Å), His322 (2.97 Å)	His322 (Pi-Pi T Shaped), Ala365 (Pi-Alkyl), Glu222 (Pi-Anion)
120	-3.9	Ala365 (2.84 Å), Asp362 (3.14 Å)	His322, His221, His248 (Pi-Alkyl), Met366, Ala365 (Alkyl)
121	-3.8	-	His221 (C-H Bond), His322, His138 (Pi-Alkyl), Ala365, Met366, Cys321 (Alkyl)
122	-4.3	-	His138, His221, His248, His274 (Pi Alkyl), Met366, Cys321 (Alkyl)
123	-4.8	-	Cys321 (Pi-Donor Hydrogen Bond), Leu318, Met317 (Pi-Alkyl), Met366 (Pi-Sulfur), Met366, Leu318, Cys321, Ile339 (Alkyl)
124	-7.0	His314 (2.61 Å), Asp223 (3.02 Å), His221 (2.80 Å), Ala169 (2.69 Å)	Leu318, Cys321, Ala169 (Pi-Alkyl), Arg338 (Pi-Cation), Met366, Met317 (Pi-Sulfur)

Cant....

125	-7.1	Ala278 (3.03 Å), His314 (2.65 Å), Asp223 (2.99 Å), Ala169 (2.68 Å), His221 (2.76 Å)	Arg338 (Pi Cation), Ala169, Leu318, Cys321 (Pi Alkyl), Met366, Met317 (Pi-Sulfur)
Std.	-7.7	His136 (3.06 Å), His138 (2.94 Å)	Met317, Leu318, Met366 (Alkyl), His322 (Pi-Pi Stacked), Met366 (Pi Alkyl), His221, His248, Cys321 (Pi-Sulfur), Cys321 (C-H Bond)

Std: Co-crystallized ligand, i.e., 2-{[1-(3,5-dimethylphenyl)-1H-imidazol-2-yl]sulfanyl}-N-hydroxyacetamide (PDB ID: 6ZJA).

glycoprotein (P-gp; ABCB1/MDR1) is an ATP-dependent efflux transporter expressed in the intestinal epithelium, liver, kidney, blood-brain barrier, and other tissues. It plays a key role in limiting drug absorption and promoting xenobiotic elimination. Compounds identified as P-gp substrates are actively transported out of cells, which can reduce intestinal absorption, decrease intracellular drug concentrations, limit brain penetration, and contribute to multidrug resistance. Therefore, P-gp substrate prediction is an important component of ADME assessment. Among the 126 phytoconstituents screened, only a relatively small fraction was predicted to be P-gp substrates, whereas the majority were classified as non-substrates (as shown in Figure 1). The P-gp substrate-positive compounds were predominantly large, highly oxygenated, glycosylated flavonoids, phenylpropanoid glycosides, and polyphenolic derivatives characterized by high MW (>450 Da), high TPSA (>140 Å^2), large numbers of HBDs and HBAs, multiple sugar moieties, and low GI absorption. Many of these molecules possess established biological activities but may exhibit reduced systemic exposure due to transporter-mediated efflux. P-gp is highly expressed at the BBB and actively excludes many xenobiotics from entering the CNS. Therefore, compounds predicted as P-gp substrates are less likely to achieve significant CNS exposure even if their physicochemical properties permit membrane permeation. The SwissADME investigation demonstrated that 92 of the 126 screened phytoconstituents exhibited favorable drug-likeness characteristics, indicating a strong potential for further development as orally active therapeutic agents.

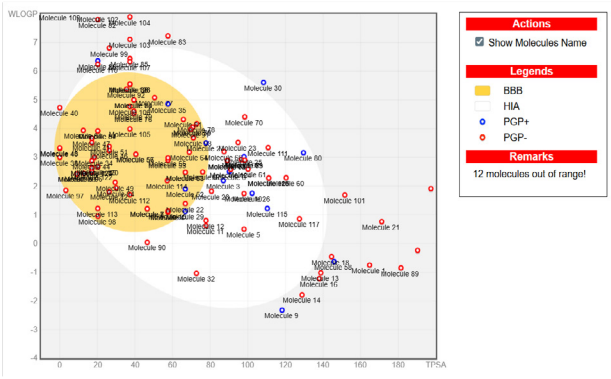

Fig. 1: BOILED-Egg (Brain Or IntestinaL EstimateD permeation) plot showing the predicted gastrointestinal absorption (HIA) and BBB permeability of the selected compounds based on the SwissADME model. The white region represents molecules with a high probability of passive HIA, while the yellow yolk indicates molecules predicted to penetrate the BBB. Blue circles denote compounds predicted to be substrates of P-gp (PGP+), whereas red circles represent non-substrates (PGP-).

Molecular Docking Studies

Computational virtual screening has evolved into a robust and economical strategy to detect prospective therapeutic leads by rapidly predicting molecular interactions between target proteins and ligand entities.[40] The present study aimed to discover newer inhibitors of urease, the key enzyme involved in *H. pylori* infection. To assess the affinity and binding modes of the chosen derivatives (92) inside the catalytic pocket of *H. pylori* urease, *in-silico* molecular docking studies were performed using AutoDock Vina.[31] Redocking of the co-crystallized ligand (PDB ID: 6ZJA) was performed to verify the reliability and precision

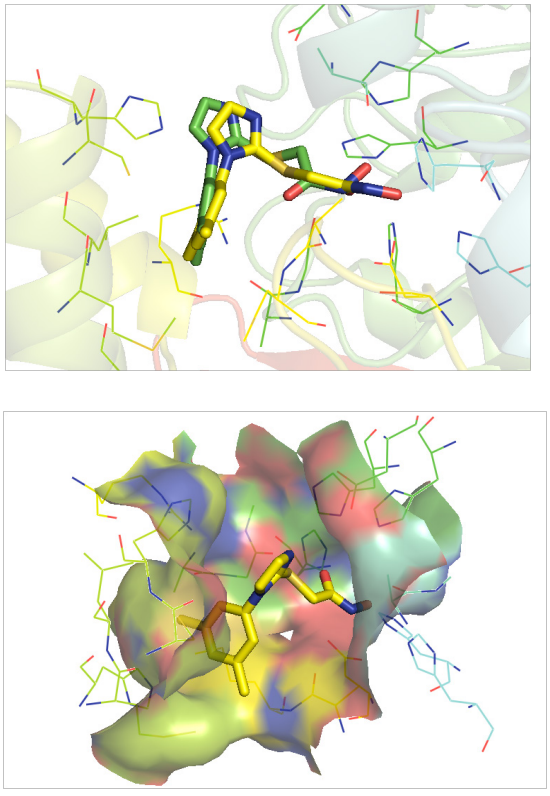

Fig. 2: Validation of the docking protocol. The docking protocol was validated via redocking the co-crystallized inhibitor of *H. pylori* urease. The re-docked ligand (yellow) produced a pose similar to that of the co-crystallized ligand (green) (LEFT) and oriented well in the active site of *H. pylori* urease (RIGHT).

of the docking protocol employed in this study. The re-docked ligand reproduced a binding orientation closely resembling the experimentally determined co-crystallized pose and exhibited a docking score (ΔG) of -7.7 kcal/mol (Figure 2). These findings confirm the suitability of the selected docking methodology for predicting the binding interactions of the screened phytoconstituents with *H. pylori* urease. The selected molecules were docked into the active site of *H. pylori* urease (PDB ID: 6ZJA) to evaluate their binding affinity and interaction patterns with the target protein. Binding free energy (docking score) serves as an important parameter for assessing the likelihood of a compound acting as a potential drug candidate, with more negative values indicating stronger and more stable protein-ligand complexes. The docking scores and the key amino acid residues involved in the hydrogen bonds as well as hydrophobic interactions of the selected compounds with the *H. pylori* urease enzyme are summarized in Table 4.

The docking scores (ΔG) ranged from -3.8 to -7.6 kcal/mol, indicating varying degrees of interaction with the catalytic pocket of urease. The co-crystallized inhibitor, 2-{[1-(3,5-dimethylphenyl)-1H-imidazol-2-yl]sulfanyl}-N-hydroxyacetamide, exhibited a docking score of -7.7 kcal/mol, which served as the reference for evaluating the binding potential of the screened phytochemicals. Among all screened compounds, sphaeranthanolide (58) showed the strongest interaction with urease, with a docking score of -7.6 kcal/mol, followed closely by (+)-catechin (115) with a docking score of -7.5 kcal/mol, scopoline (13) (-7.4 kcal/mol), epicatechin (6) (-7.4 kcal/mol), and (+)-hardwickiic acid (77) (-7.4 kcal/mol). Other compounds exhibiting excellent binding energies included sakuranetin (67) (-7.3 kcal/mol), 4',5,7-trihydroxy-3-methoxyflavone (61) (-7.2 kcal/mol), labda-8(17),13-dien-15-olide (78) (-7.2 kcal/mol), (S)-5,4'-dihydroxy-7-methoxyflavone (65) (-7.2 kcal/mol), luteolin (125) (-7.1 kcal/mol), taxifolin (117) (-7.1 kcal/mol), naringenin (3) (-7.1 kcal/mol), isorhamnetin (60) (-7.1 kcal/mol), and methyl dodovisate A (88) (-7.1 kcal/mol). These values approach the binding affinity of the reference, suggesting a strong capacity to occupy and stabilize within the urease active site. These compounds were further analysed in detail using PyMOL and Discovery Studio.

The molecular docking analysis revealed that several phytoconstituents exhibited strong binding affinity toward the active site of *H. pylori* urease through a combination of hydrogen bonding, hydrophobic interactions, Pi-Pi stacking, Pi-alkyl contacts, and Pi-sulfur interactions. Among the investigated compounds, sphaeranthanolide (58) established multiple hydrogen bonds with Gly279, Ala169, Asn168, and Asp165, while additional alkyl and Pi-alkyl interactions with Cys321, Ala169, and His322

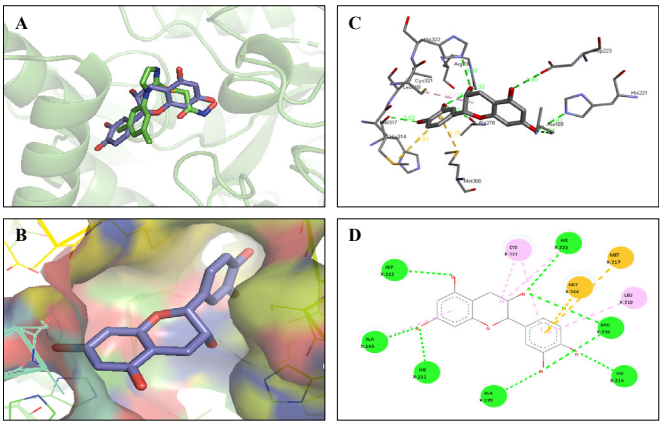

Fig. 4: Interaction analysis of (+)-catechin (115) with urease. A. Overlay of the docked pose of 115 (purple) with that of the co-crystallized ligand (green). B. orientation the active site. C. 3D docked pose. D. 2D docked pose.

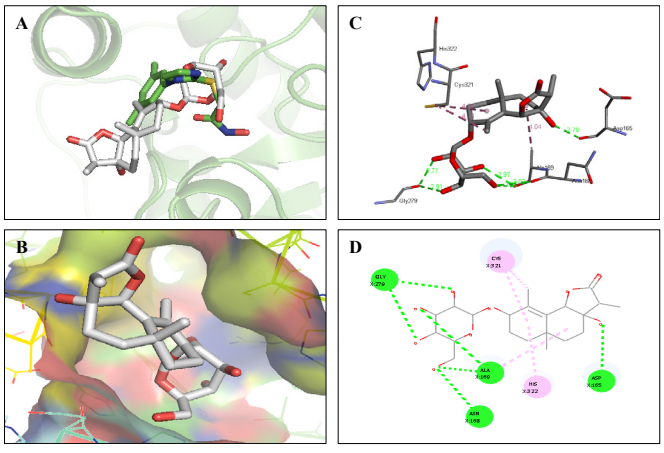

Fig. 3: Interaction analysis of sphaeranthanolide (58) with urease. A. Overlay of the docked pose of sphaeranthanolide (white) with that of the co-crystallized ligand (green). B. orientation of sphaeranthanolide in the active site of urease. C. 3D docked pose. D. 2D docked pose in the active site of urease.

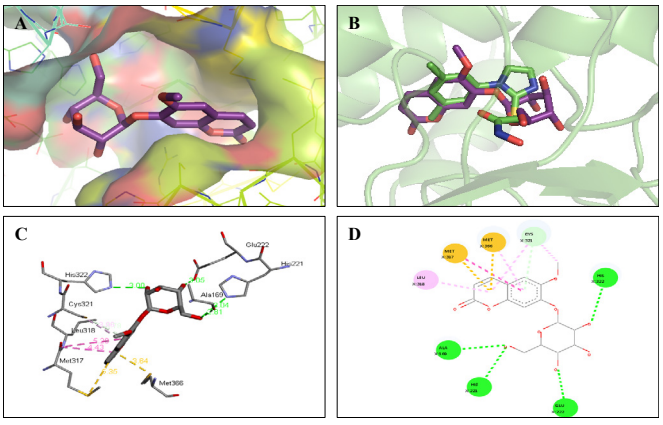

Fig. 5: Interaction analysis of scopoline (13) with urease. A. orientation in the active site. B. Overlay of the docked pose of scopoline (purple) with that of the co-crystallized ligand (green). C. 3D docked pose. D. 2D docked pose of scopoline showing hydrogen bond and hydrophobic interactions.

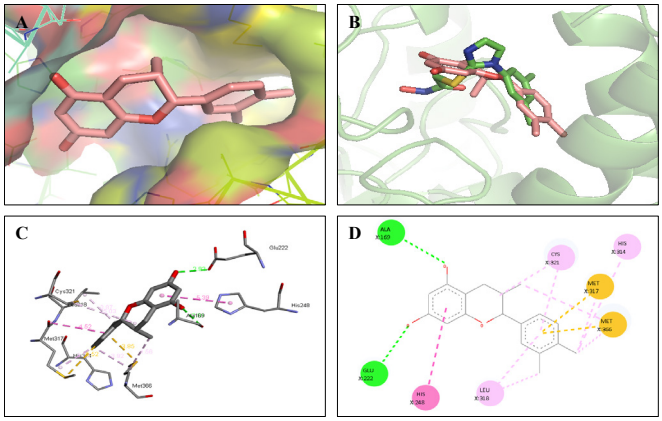

Fig. 6: Interaction analysis of epicatechin (6) with urease. A. orientation in the active site. B. Overlay of the docked pose of epicatechin (pink) with that of the co-crystallized ligand (green). C. 3D docked pose. D. 2D docked pose of epicatechin showing hydrogen bond and hydrophobic interactions.

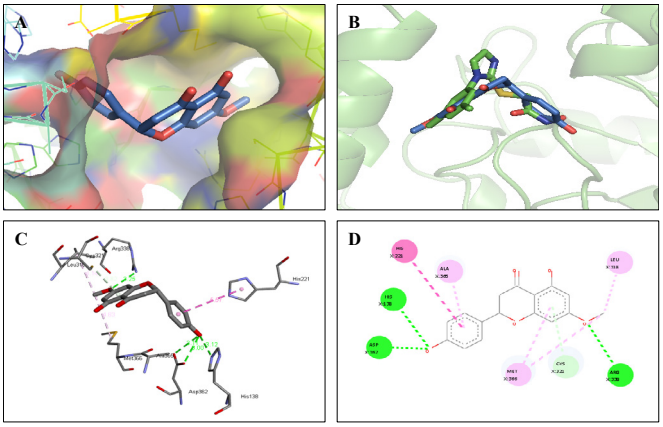

Fig. 8: Interaction analysis of sakuranetin (67) with urease. A. orientation in the active site. B. Overlay of the docked pose of scopoline (blue) with that of the co-crystallized ligand (green). C. 3D docked pose. D. 2D docked pose of sakuranetin showing hydrogen bond and hydrophobic interactions.

contributed to the stabilization of the ligand within the active site. The involvement of Asp165 and Gly279, which are located in proximity to the catalytic environment, suggests that sphaeranthanolide may effectively interfere with the enzymatic activity of urease (Figure 3).

(+)-Catechin (115) formed an extensive hydrogen bonding network involving Ala169, His221, Asp223, Ala278, His314, Arg338, and His322, indicating a strong interaction profile within the binding cavity. Furthermore, Pi-alkyl interactions with Cys321, His322, Leu318, and Ala169, together with Pi-sulfur contacts involving Met317 and Met366, enhanced the overall binding stability (Figure 4).

Scopoline (13) displayed hydrogen bonds with Ala169, His221, Glu222, and His322. The ligand also formed amide-Pi stacked interactions with Met317, Pi-alkyl interactions with Leu318, Met366, and Cys321, and Pi-sulfur interactions with Met317, Met366, and Cys321, highlighting the importance of hydrophobic interactions in maintaining complex stability (Figure 5).

Epicatechin (6) established hydrogen bonds with Ala169 and Glu222, while the His248 residue participated in Pi-Pi stacking interactions. Additional hydrophobic contacts involving Leu318, His314, Met317, Met366, and Cys321 further contributed to the favorable binding orientation observed for this compound (Figure 6).

(+)-Hardwickiic acid (77) interacted through hydrogen bonding with Asp362 and Gly279, accompanied by C-H Bonding involving His314. The presence of Pi-alkyl interactions with His322, Cys321, and Leu318, together with Pi-sulfur interactions with Met317 and Met366, reinforced its binding within the urease active site (Figure 7).

Among the flavonoid derivatives, sakuranetin (67) formed hydrogen bonds with His138, Asp362, and Arg338, while

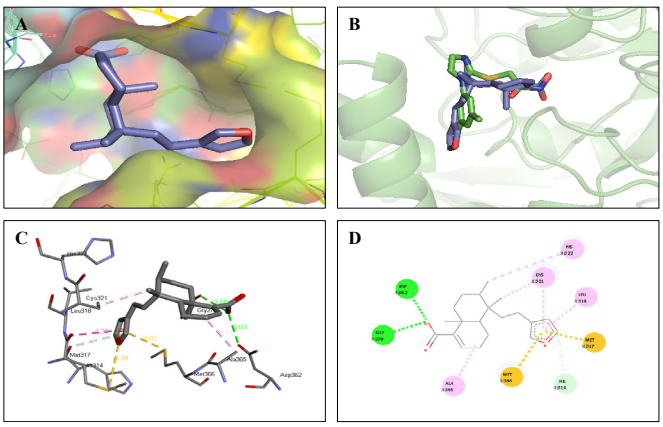

Fig. 7: Interaction analysis of (+)-hardwickiic acid (77) with urease. A. orientation in the active site. B. Overlay of the docked pose of (+)-hardwickiic acid (purple) with that of the co-crystallized ligand (green). C. 3D docked pose. D. 2D docked pose of (+)-hardwickiic acid in the active site of urease.

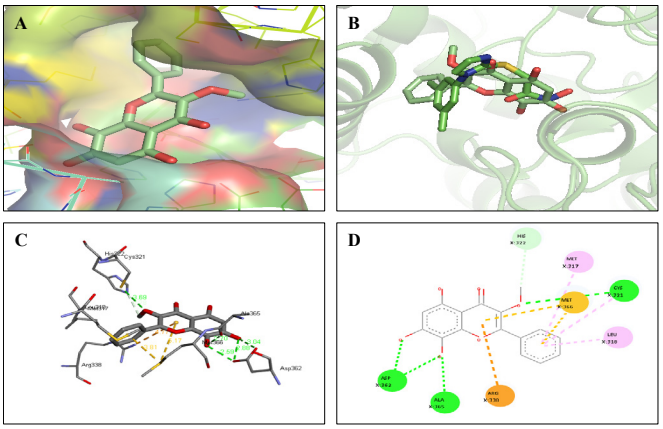

Fig, 9: Interaction analysis of 4',5,7-trihydroxy-3-methoxyflavone (61) with urease. A. orientation of in the active site. B. Overlay of the docked pose of 4',5,7-trihydroxy-3-methoxyflavone with that of the co-crystallized ligand. C. 3D docked pose. D. 2D docked pose in the active site of urease.

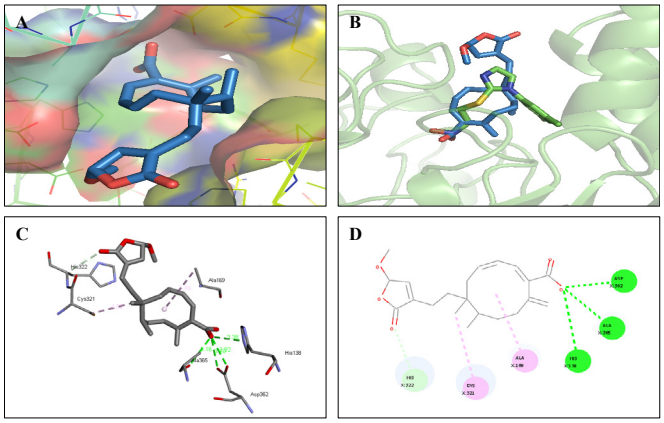

Fig. 10: Interaction analysis of labda-8(17),13-dien-15-olide (78) with urease. A. orientation in the active site. B. Overlay of the docked pose of labda-8(17),13-dien-15-olide (blue) with that of the co-crystallized ligand (green). C. 3D docked pose. D. 2D docked pose in the active site of urease.

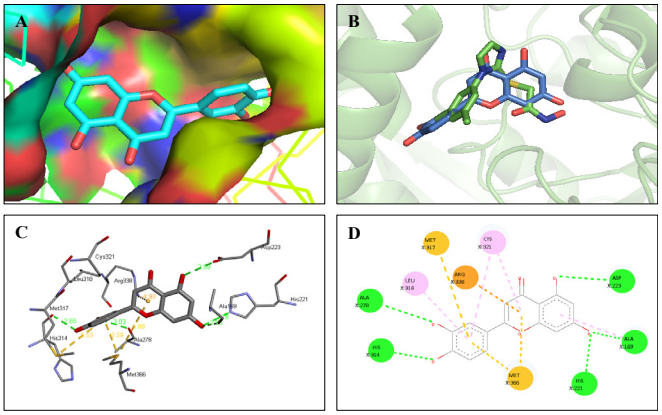

Fig. 12: Interaction analysis of luteolin (125) with urease. A. orientation in the active site of urease. B. Overlay of the docked pose of luteolin (blue) with that of the co-crystallized ligand (green). C. 3D docked. D. 2D docked pose showing hydrogen bond and hydrophobic interactions.

Cys321 contributed through Pi-donor hydrogen bonding and Pi-sulfur interactions. Additional hydrophobic contacts involving His221, Leu318, Met366, and Ala365 facilitated stabilization of the complex (Figure 8).

The flavone derivative 4',5,7-trihydroxy-3-methoxyflavone (61) showed hydrogen bonds with Asp362, Ala365, and Cys321, whereas Arg338 participated in Pi-cation interactions. Moreover, Pi-alkyl interactions involving Met317, Cys321, and Leu318, together with C-H Bonding with His322, contributed to its favorable binding profile (Figure 9).

Labda-8(17),13-dien-15-olide (78) established hydrogen bonds with Asp362, Ala365, and His138. Additional alkyl interactions involving Ala169 and Cys321, along with C-H Bonding with His322, suggested a stable accommodation within the active site of urease enzyme (Figure 10).

(S)-5,4'-Dihydroxy-7-methoxyflavone formed hydrogen bonding interactions with Asn168, while C-H Bonds were observed with His221 and His248. Furthermore, Pi-anion interactions with Glu222 and Asp223, together with extensive Pi-alkyl interactions involving His322, His248, His274, His136, His138, Ala169, and Ala365, contributed to its enhanced binding affinity (Figure 11).

Luteolin (125) established multiple hydrogen bonds with Ala278, His314, Asp223, Ala169, and His221, in addition to interactions with Arg338 and His322. The binding was further stabilized through Pi-cation interactions with Arg338, Pi-alkyl interactions involving Leu318, Cys321, and Ala169, and Pi-sulfur interactions with Met317 and Met366 in the active site of the urease enzyme (Figure 12).

Taxifolin (117) formed hydrogen bonds with Ala365, Ala169, Asp223, Glu222, and His322, while His322 contributed through Pi-Pi T-shaped interactions. Additional Pi-alkyl contacts involving Ala365 and Pi-anion

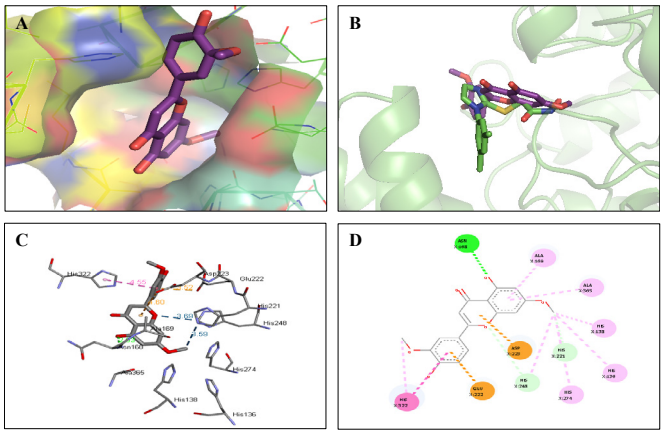

Fig. 11: Interaction analysis of (S)-5,4'-dihydroxy-7-methoxyflavone (65) with urease. A. orientation in the active site of urease. B. Overlay of the docked pose of (S)-5,4'-dihydroxy-7-methoxyflavone (purple) with that of the co-crystallized ligand (green). C. 3D docked pose. D. 2D docked pose in the active site of urease.

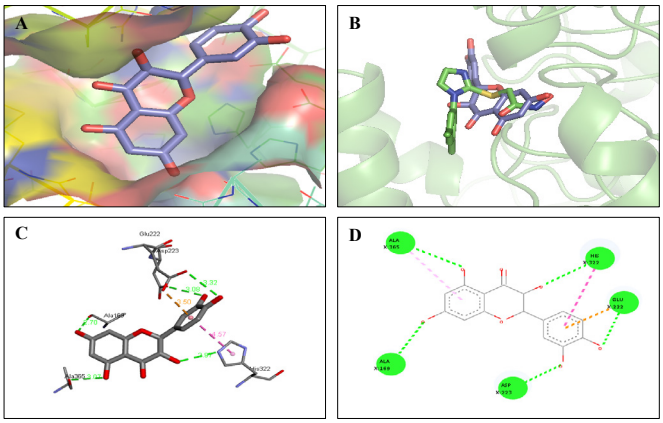

Fig. 13: Interaction analysis of taxifolin (117) with urease. A. orientation in the active site of urease. B. Overlay of the docked pose of taxifolin (purple) with that of the co-crystallized ligand (green). C. 3D docked pose. D. 2D docked pose showing hydrogen bond and hydrophobic interactions.

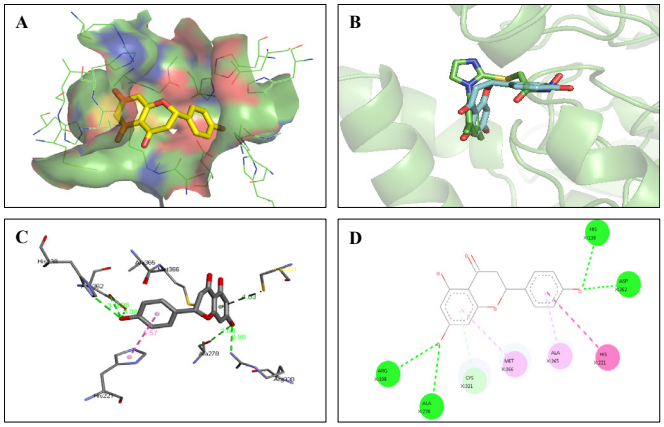

Fig. 14: Interaction analysis of naringenin (3) with urease. A. orientation in the active site of urease. B. Overlay of the docked pose of naringenin (blue) with that of the co-crystallized ligand (green). C. 3D docked pose. D. 2D docked pose showing hydrogen bond and hydrophobic interactions.

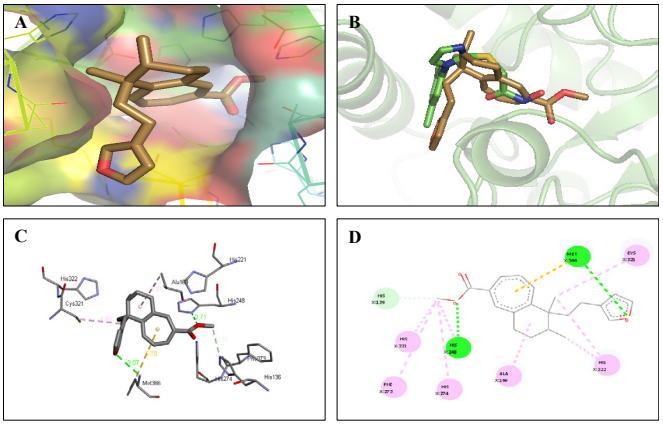

Fig. 16: Interaction analysis of methyl dodovisate A (88) with urease. A. orientation in the active site of urease. B. Overlay of the docked pose of methyl dodovisate A (brown) with that of the co-crystallized ligand (green). C. 3D docked pose. D. 2D docked pose showing hydrogen bond and hydrophobic interactions.

interactions with Glu222 further strengthened the protein-ligand complex (Figure 13).

Naringenin (3) interacted with Arg338, Ala278, Asp362, and His138 through hydrogen bonding, whereas hydrophobic stabilization was provided by Cys321, His221, Ala365, and Met366 through Pi-donor hydrogen bonding, Pi-Pi T-shaped, Pi-alkyl, and Pi-sulfur interactions (Figure 14).

Isorhamnetin (60) formed hydrogen bonds with Asn168 and Asp362, C-H bonding with His248, and Pi-anion interactions involving Glu222 and Asp223. Furthermore, Pi-alkyl interactions with Ala365 and His322, together with Pi-Pi T-shaped interactions involving His322, contributed significantly to complex stabilization (Figure 15).

Methyl dodovisate A (88) formed hydrogen bonds with His248 and Met366, while extensive Pi-alkyl interactions involving His221, His248, His274, His322, and Phe273, as well as alkyl interactions with Ala169 and Cys321, contributed to the favorable binding orientation. The presence of Pi-sulfur interactions with Met366 further enhanced the stability of the complex (Figure 16).

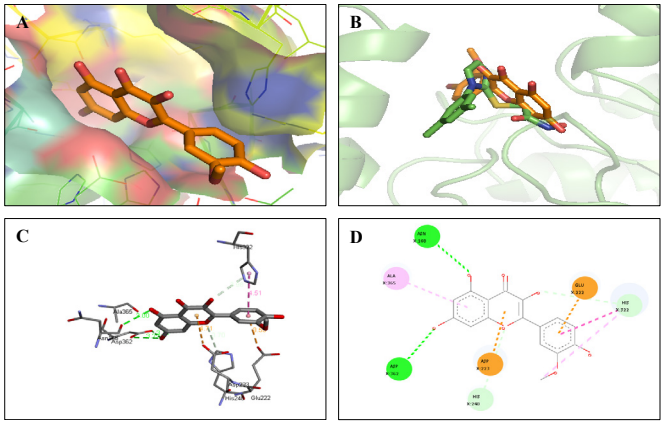

Fig. 15: Interaction analysis of isorhamnetin (60) with urease. A. orientation in the active site of urease. B. Overlay of the docked pose of isorhamnetin (orange) with that of the co-crystallized ligand (green). C. 3D docked pose. D. 2D docked pose showing hydrogen bond and hydrophobic interactions.

Toxicity Prediction

The safety profile of the fourteen lead compounds identified through molecular docking studies was evaluated using the pkCSM (https://biosig.lab.uq.edu.au/pkcsm/) toxicity prediction platform. Several important toxicological endpoints, including AMES toxicity (mutagenicity), maximum tolerated dose, hERG channel inhibition (cardiotoxicity), oral acute and chronic toxicity, hepatotoxicity, skin sensitization, *Tetrahymena pyriformis* toxicity, and minnow toxicity, were assessed to determine the suitability of the compounds for further drug development (Table 5).

The AMES mutagenicity model revealed that naringenin (3) and 4',5,7-trihydroxy-3-methoxyflavone (61) were predicted to be mutagenic, whereas the remaining 12 molecules were classified as non-mutagenic. The predominance of non-mutagenic compounds among the selected leads indicates a generally favorable genetic safety profile. Mutagenicity is a critical parameter during early-stage drug discovery because mutagenic compounds may pose risks of DNA damage and carcinogenicity. Therefore, the Ames predictions for compounds 3 and 61 suggest that additional experimental evaluation would be required before considering these molecules for further development. The predicted maximum tolerated dose values ranged from -0.294 to 1.039 log mg/kg/day. Among the evaluated compounds, (+)-hardwickiic acid (77) exhibited the highest maximum tolerated dose (1.039 log mg/kg/day), indicating a potentially wider safety margin, followed by isorhamnetin (60) (0.738 log mg/kg/day), scopoline (13) (0.700 log mg/kg/day), and

Table 5: *In-silico* toxicity prediction of the lead compounds against *H. pylori* urease using the pkCSM toxicity assessment platform.

Ligand	*AMES*	*MTD*	*hERG I*	*hERG II*	*LD_{50}*	*LOAEL*	*HepTox*	*SS*	*TPT*	*MTox*
3	Yes	0.499	No	No	2.010	2.270	No	No	0.532	1.294
6	No	-0.209	No	Yes	2.339	1.683	No	No	0.694	1.972
13	No	0.700	No	No	2.323	3.191	Yes	No	0.285	3.056
58	No	0.148	No	No	2.616	2.436	No	No	0.285	4.441
60	No	0.738	No	Yes	2.379	2.559	No	No	0.318	1.646
61	Yes	0.655	No	Yes	2.416	2.380	No	No	0.291	0.985
65	No	0.521	No	Yes	2.587	1.576	No	No	0.418	0.402
67	No	-0.294	No	No	2.332	1.647	No	No	0.365	1.893
77	No	1.039	No	No	2.555	1.949	No	No	1.486	-0.097
78	No	0.332	No	No	2.601	1.630	No	No	0.371	0.156
88	No	0.098	No	No	2.414	1.614	No	No	1.730	-0.896
115	No	0.244	No	No	2.387	1.882	No	No	0.605	2.869
117	No	0.247	No	No	2.333	1.955	No	No	0.389	3.368
125	No	0.564	No	No	2.453	1.537	No	No	0.428	1.346

Abbreviations: AMES: Ames mutagenicity; MTD: Maximum tolerated dose (in humans) (log mg/kg/day); hERG I: hERG I inhibition; hERG II: hERG II inhibition; LD50: Oral rat acute toxicity (mol/kg); LOAEL, Lowest observed adverse effect level (log mg/kg_bw/day); HepTox: Hepatotoxicity; SS: Skin sensitisation; TPT: Tetrahymena pyriformis toxicity; MTox: Minnow toxicity.

4',5,7-trihydroxy-3-methoxyflavone (61) (0.655 log mg/kg/day). The observed maximum tolerated dose values suggest acceptable tolerance levels for most of the selected lead compounds. Cardiotoxicity is one of the major causes of drug attrition during clinical development. Therefore, inhibition of the hERG potassium channel was assessed. None of the lead compounds were predicted to inhibit the hERG I channel, indicating a low risk of severe cardiac toxicity. However, epicatechin (6), isorhamnetin (60), 4',5,7-trihydroxy-3-methoxyflavone (61), and (S)-5,4'-dihydroxy-7-methoxyflavone (65) were predicted as hERG II inhibitors. Although hERG II inhibition is generally considered less critical than hERG I inhibition, these compounds may require further cardiotoxicity assessment during subsequent stages of development. The predicted oral rat acute toxicity (LD_{50}) values ranged from 2.010 to 2.616 mol/kg, indicating relatively low acute toxicity for all compounds. Among the lead molecules, sphaeranthanolide (58) exhibited the highest LD_{50} value (2.616 mol/kg), followed by labda-8(17),13-dien-15-olide (78) (2.601 mol/kg) and (S)-5,4'-dihydroxy-7-methoxyflavone (65) (2.587 mol/kg). Higher LD_{50} values generally indicate lower acute toxicity, suggesting favorable safety characteristics for these compounds. Similarly, the oral rat chronic toxicity (LOAEL) values ranged between 1.537 and 3.191 log mg/kg_bw/day. Scopoline (13) demonstrated the highest LOAEL value (3.191 log mg/kg_bw/day), suggesting comparatively lower chronic toxicity, whereas luteolin (125) exhibited the lowest LOAEL value (1.537 log mg/kg_bw/day). Still, all compounds showed values within an acceptable range for naturally derived bioactive molecules. Evaluation of hepatotoxicity showed that all compounds were predicted to be non-hepatotoxic except scopoline (13), which demonstrated a positive hepatotoxicity prediction. The environmental toxicity assessment demonstrated variability among the lead molecules. Tetrahymena pyriformis toxicity values ranged from 0.285 to 1.730, with methyl dodovisate A (88) showing the highest predicted toxicity (1.730), followed by (+)-hardwickiic acid (77) (1.486). Minnow toxicity values ranged from -0.896 to 4.441, with sphaeranthanolide (58) exhibiting the highest predicted aquatic toxicity (4.441), followed by taxifolin (117) (3.368) and scopoline (13) (3.056). Although these parameters are primarily used to assess environmental safety rather than therapeutic risk, they provide valuable information regarding the ecological impact of potential drug candidates. Overall, the toxicity prediction results suggest that the majority of the selected lead compounds possess favorable safety profiles.

DFT Calculations

DFT calculations were performed to investigate the electronic properties and chemical reactivity of sphaeranthanolide. The optimized molecular geometry, frontier molecular orbital distributions, and global reactivity descriptors were analyzed to gain insights into the potential inhibitory behavior of the compound against *H. pylori* urease. The optimized geometry

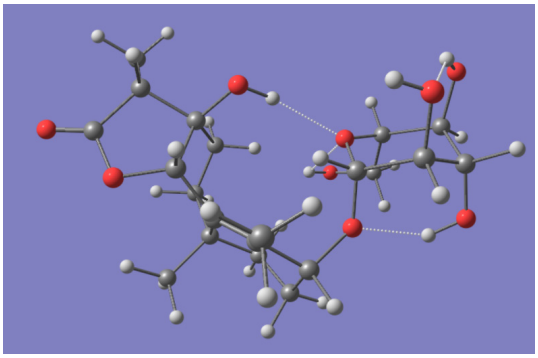

Fig. 17: Optimized molecular structure of sphaeranthanolide adopted by the molecule after geometry optimization.

of sphaeranthanolide (Figure 17) revealed a stable three-dimensional conformation characterized by a sesquiterpene lactone core attached to a glycosidic moiety. The molecule retained its structural integrity without any apparent steric hindrance, indicating that the optimized structure represented an energetically favorable configuration. The presence of multiple hydroxyl groups and carbonyl functionalities provides several potential sites for intermolecular interactions, particularly hydrogen bonding with amino acid residues within the urease active site.

The frontier molecular orbital analysis showed that the HOMO electron density (Figure 18) was predominantly distributed over the sesquiterpene lactone framework and oxygen-containing functional groupsof sphaeranthanolide. These regions are considered electron-rich sites and are more likely to participate in electron donation and electrophilic interactions. In contrast, the LUMO electron density (Figure 19) was localized mainly around the oxygenated portions of the molecule, indicating potential electron-accepting regions involved in nucleophilic interactions. The spatial separation between the HOMO and LUMO orbitals suggests intramolecular charge transfer characteristics, which may influence the interaction of the ligand with biological macromolecules. The calculated HOMO and LUMO energies were found to be -11.018 eV and -7.130 eV, respectively. The HOMO-LUMO energy gap (ΔE) was determined to be 3.888 eV. The moderate energy gap indicates that sphaeranthanolide possesses an appropriate balance between kinetic stability and chemical reactivity. Molecules exhibiting relatively lower energy gaps generally demonstrate enhanced electron transfer capability and improved interactions with target proteins. Therefore, the observed HOMO-LUMO energy gap (ΔE) value suggests that sphaeranthanolide may readily participate in stabilizing interactions with the urease active site.

Based on Koopmans' theorem, several global reactivity descriptors were calculated from the frontier orbital energies (Table 6). The ionization potential (I) and electron affinity (A) were estimated to be 11.018 eV and 7.130 eV, respectively. The relatively high ionization potential reflects the resistance of the molecule toward electron removal, while the substantial electron affinity indicates its tendency to accept electrons during intermolecular interactions. The chemical hardness (η) of sphaeranthanolide was calculated as 1.944 eV, whereas the chemical softness (S) was 0.257 eV^{-1}. The moderate hardness value suggests sufficient structural stability, while the softness value indicates the ability of the molecule to undergo polarization in response to the surrounding environment, thereby facilitating favorable interactions with receptor residues. The electronegativity (χ) and chemical potential (μ) values were determined to be 9.074 eV and -9.074 eV, respectively. The negative chemical potential signifies the intrinsic stability of the molecule and its tendency to attract electrons from the surrounding environment. Furthermore, the electrophilicity index (ω) was calculated to be 21.177 eV, indicating a pronounced electrophilic character and a strong propensity to accept electrons from electron-rich sites within the biological target.

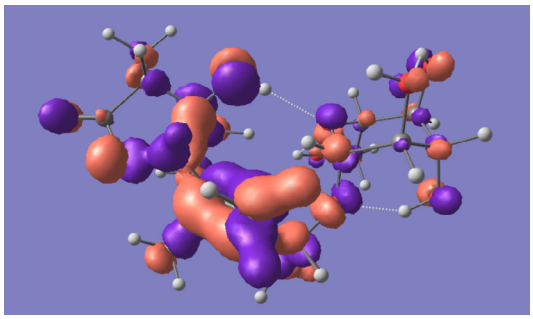

Fig. 18: Graphical representation of the HOMO electron density distribution showing the electron-donating regions localized predominantly over the sesquiterpene lactone framework and oxygen-containing functionalities.

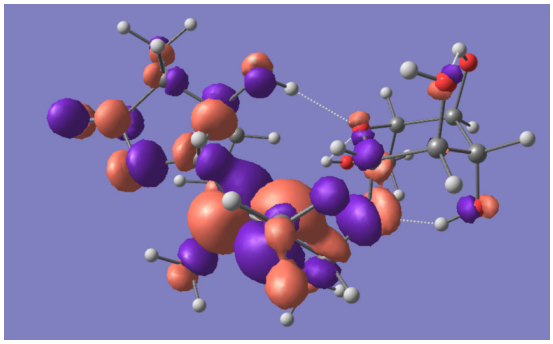

Fig. 19: Graphical representation of the LUMO electron density distribution highlighting the electron-accepting regions of sphaeranthanolide involved in inter-molecular charge-transfer interactions.

Table 6: Global reactivity descriptors of sphaeranthanolide (58) calculated using DFT analysis.

Parameter	*Symbol*	*Value*
HOMO energy	EHOMO	-11.018 eV
LUMO energy	ELUMO	-7.130 eV
Energy gap	ΔE	3.888 eV
Ionization potential	I	11.018 eV
Electron affinity	A	7.130 eV
Chemical hardness	η	1.944 eV
Chemical softness	S	0.257 eV^{-1}
Electronegativity	χ	9.074 eV
Chemical potential	μ	-9.074 eV
Electrophilicity index	ω	21.177 eV

MD Simulations

To validate the stability of docked sphaeranthanolide-urease complex under physiological conditions, a 100 ns MD simulation was performed using Desmond. The RMSD profile provides insight into the structural stability of the protein and ligand during the simulation period. As illustrated in Figure 20, the Cα backbone RMSD of *H. pylori* urease exhibited an initial equilibration phase during the early stage of the simulation, followed by stabilization throughout the remaining trajectory. The average protein RMSD value was 3.38 Å, ranging from 2.39 to 4.07 Å, indicating that the protein maintained its overall conformational integrity without undergoing significant structural perturbations. Similarly, the ligand RMSD relative to the protein backbone demonstrated an average value of 2.78 Å (1.23-4.19 Å), suggesting that sphaeranthanolide remained firmly accommodated within the urease binding cavity throughout the simulation. Furthermore, the ligand RMSD with respect to its initial conformation exhibited a substantially lower average value of 0.68 Å, reflecting minimal internal conformational rearrangements and highlighting the structural stability of the bound ligand. Collectively, these observations suggest the formation of a stable protein-ligand complex during the entire simulation period. Residue-wise flexibility of urease in the presence of sphaeranthanolide was assessed through RMSF analysis. As depicted in (Figure 21) , most amino acid residues displayed fluctuations below 3.0 Å, indicating limited mobility and preservation of protein structural integrity. Higher RMSF values were predominantly confined to terminal and loop regions, which are intrinsically flexible segments of proteins. Importantly, residues constituting the active site region exhibited relatively low fluctuations, demonstrating that ligand binding contributed to stabilization of the catalytic pocket. The restricted mobility of these residues further supports the ability of sphaeranthanolide to maintain

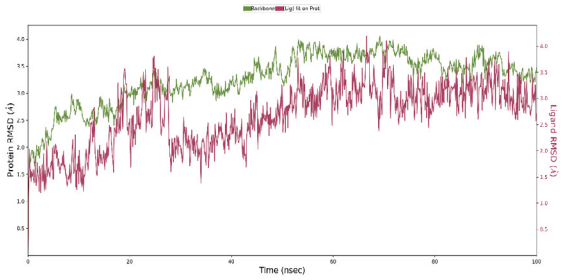

Fig. 20: RMSD plots of the sphaeranthanolide-urease complex during the 100 ns MD simulation. The plots represent the RMSD profiles of the protein backbone (Cα atoms) and ligand with respect to the initial structure, demonstrating the overall stability of the complex throughout the simulation period.

favorable interactions with urease throughout the simulation.

The persistence and nature of interactions between sphaeranthanolide and urease were investigated using the protein-ligand interaction timeline generated by Desmond (Schrödinger, Inc.). The interaction map (Figure 22) revealed that hydrogen bonding played a predominant role in stabilizing the complex. Among the interacting residues, Asp362 exhibited the highest interaction occupancy (>100%), indicating the presence of multiple hydrogen bond contacts during the simulation trajectory. Significant hydrogen bond interactions were also observed with Glu222 (59.34%), Gly279 (37.16%), and Arg338 (32.97%), suggesting their critical involvement in ligand recognition and retention within the active site. Additional intermittent interactions involving Asn168, Asp165, His221, His248, and His274 residues further strengthened the interaction network. Hydrophobic contacts also contributed to the stability of the complex. Residues Leu318 (13.89%), Cys321 (12.09%), Ala365 (7.69%), and Met366 (6.89%) established nonpolar interactions with sphaeranthanolide, thereby facilitating favorable van der Waals contacts and improving ligand accommodation within the binding pocket (Figure 22).

To quantify the contribution of individual residues toward

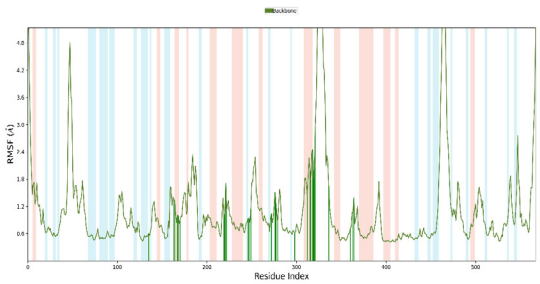

Fig. 21: RMSF analysis of amino acid residues of sphaeranthanolide-urease complex during the 100 ns MD simulation. Lower fluctuations observed for active-site residues indicate stabilization of the catalytic pocket upon ligand binding.

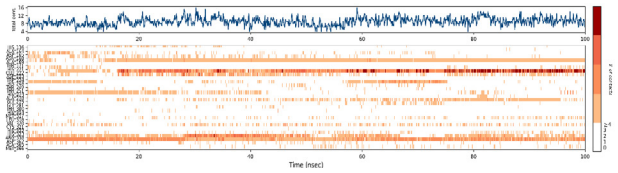

Fig. 22: Protein-ligand interaction timeline illustrating the interactions formed between sphaeranthanolide and *H. pylori* urease during the MD simulation. Hydrogen bonds, hydrophobic contacts, water bridges, and ionic interactions are represented as a function of simulation time.

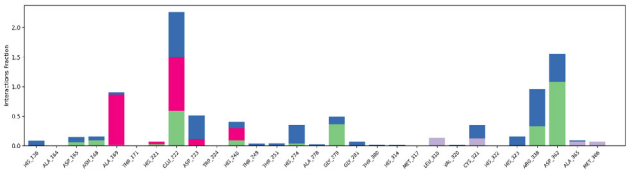

Fig. 23: Interaction occupancy profile showing the percentage contribution of individual amino acid residues toward stabilization of the sphaeranthanolide-urease complex throughout the 100 ns simulation. Asp362, Glu222, Gly279, and Arg338 exhibited the highest interaction frequencies.

ligand stabilization, interaction occupancy analysis was performed (Figure 23). The results confirmed that Asp362, Glu222, Gly279, and Arg338 represented the principal residues involved in maintaining stable contacts with sphaeranthanolide throughout the simulation.

The identification of lead molecules represents a critical step in the drug discovery process, enabling the selection of compounds with favorable binding characteristics for further optimization and biological evaluation. In the present study, molecular docking analysis of 92 phytoconstituents against *H. pylori* urease revealed several compounds with remarkable binding affinities and favorable interaction profiles within the enzyme active site. Based on docking scores, interaction with catalytically important amino acid residues, and the overall stability of the ligand-protein complexes, 14 compounds were identified as potential lead molecules. The selected lead compounds include sphaeranthanolide (58), (+)-catechin (115), scopoline (13), epicatechin (6), (+)-hardwickiic acid (77), sakuranetin (67), 4',5,7-trihydroxy-3-methoxyflavone (61), labda-8(17),13-dien-15-olide (78), (S)-5,4'-dihydroxy-7-methoxyflavone (65), luteolin (125), taxifolin (117), naringenin (3), isorhamnetin (60), and methyl dodovisate A (88). These compounds exhibited docking scores ranging from -7.1 to -7.6 kcal/mol, approaching the binding affinity of the reference inhibitor (-7.7 kcal/mol), indicating their strong potential to inhibit urease activity. Among the identified leads, sphaeranthanolide exhibited the highest binding affinity (-7.6 kcal/mol), followed by (+)-catechin, scopolin, epicatechin, and (+)-hardwickiic acid, which demonstrated docking scores between -7.4 and -7.5 kcal/mol. These compounds formed multiple hydrogen bonds and hydrophobic interactions with key active-site residues, contributing to stable enzyme-ligand complexes. Particularly, residues such as Asp223, Glu222, His221, His314, Cys321, His322, Arg338, Asp362, Ala169, and Met366 were repeatedly involved in ligand recognition and stabilization, highlighting their importance in urease inhibition. Chemical classification of the lead molecules revealed that the majority belonged to the flavonoid class, including (+)-catechin, epicatechin, sakuranetin, 4',5,7-trihydroxy-3-methoxyflavone, (S)-5,4'-dihydroxy-7-methoxyflavone, luteolin, taxifolin, naringenin, and isorhamnetin. The predominance of flavonoids among the top-ranked compounds suggests that polyphenolic scaffolds are particularly favorable for binding within the urease catalytic pocket. The second major group consisted of terpenoids, represented by sphaeranthanolide, (+)-hardwickiic acid, labda-8(17),13-dien-15-olide, and methyl dodovisate A. These compounds exhibited extensive hydrophobic interactions with residues lining the active-site cavity, thereby enhancing binding stability. Sphaeranthanolide, a sesquiterpene lactone, displayed the strongest affinity among all screened compounds, whereas (+)-hardwickiic acid and labda-8(17),13-dien-15-olide, both diterpenoid derivatives, demonstrated favorable interaction patterns comparable to several flavonoids. Methyl dodovisate A (a diterpenoid), also exhibited significant binding affinity and extensive hydrophobic interactions with the enzyme. In addition, scopolin, a coumarin glycoside, emerged as a promising lead molecule. The compound established multiple hydrogen-bonding interactions and hydrophobic contacts with important active-site residues, indicating effective accommodation within the urease binding pocket. The identification of scopolin among the lead compounds suggests that coumarin derivatives may also serve as valuable scaffolds for urease inhibition.

CONCLUSION

The present study successfully demonstrated the utility of a docking-guided computational strategy for the identification of natural urease inhibitors with potential application in the management of *H. pylori* infections. Among the 126 phytoconstituents screened, 92 compounds exhibited favorable drug-likeness properties, indicating their suitability for further investigation. Molecular docking identified several compounds with strong binding affinity toward *H. pylori* urease, with sphaeranthanolide emerging as the most promising candidate. The superior docking performance of sphaeranthanolide was supported by its ability to establish multiple stabilizing interactions with key active-site residues. Subsequent MD simulations confirmed the dynamic stability of the sphaeranthanolide-urease complex under physiological conditions, while DFT analysis revealed favorable electronic characteristics associated with molecular recognition and chemical

reactivity. The convergence of evidence obtained from these complementary computational approaches strengthens the potential of sphaeranthanolide as a promising lead molecule for the development of novel anti-*H. pylori* therapeutics targeting urease. Although the present investigation provides valuable insights into the anti-urease potential of selected phytochemicals, the findings are based exclusively on *in-silico* approaches. Therefore, further in vitro urease inhibition assays, anti-*H. pylori* studies, and *in vivo* evaluations are warranted to validate the therapeutic efficacy and safety of the identified lead compounds. Nevertheless, the outcomes of this study contribute to the growing body of evidence supporting natural products as valuable sources of novel anti-H. *pylori* agents and establish a foundation for future experimental and translational research aimed at combating antibiotic-resistant *H. pylori* infections.

LIMITATIONS OF THE STUDY

The present study utilized an inclusive computational approach to identify potential natural urease inhibitors against *H. pylori*; however, certain limitations of the study should be acknowledged. The investigation was conducted entirely using *in-silico* techniques, including drug-likeness prediction, molecular docking, toxicity assessment, DFT calculations, and MD simulations. While these approaches are widely recognized as effective tools in early-stage drug discovery, they cannot fully reproduce the complexity of biological systems. Consequently, the predicted binding affinities, inhibitory activities, pharmacokinetic properties, and toxicity profiles require confirmation through experimental studies such as in vitro enzyme assays, cell culture investigations, and in vivo evaluations. Molecular docking predicts protein-ligand interactions based on static protein structures and scoring functions, which may not always accurately reflect actual biological binding behavior. Similarly, ADMET and toxicity predictions are dependent on computational algorithms and available datasets, and therefore may differ from real biological responses. DFT calculations provide valuable information regarding molecular electronic properties and reactivity but are performed under idealized theoretical conditions that do not completely account for physiological environments. In addition, the study focused only on phytoconstituents reported from selected medicinal plants with documented anti-*H. pylori* activity, potentially excluding other promising natural compounds.

AI DISCLOSURE STATEMENT

During the preparation of this manuscript, the authors used Grammarly and ChatGPT (v GPT-4.5) for language editing, grammar improvement, and language checking. After its use, the authors thoroughly reviewed, verified, and revised all AI-assisted content to ensure accuracy and originality. The authors take full responsibility for the integrity and final content of the published article.

REFERENCES

1. Eusebi LH, Zagari RM, Bazzoli F. Epidemiology of Helicobacter pylori infection. Helicobacter. 2014;19 Suppl 1:1-5. doi: 10.1111/hel.12165.
2. Ali A, AlHussaini KI. Helicobacter pylori: A contemporary perspective on pathogenesis, diagnosis and treatment strategies. Microorganisms. 2024;12(1):222. doi: 10.3390/microorganisms12010222.
3. Yi M, Chen S, Yi X, Zhang F, Zhou X, Zeng M, Song H. Helicobacter pylori infection process: From the molecular world to clinical treatment. Front Microbiol. 2025;16:1541140. doi: 10.3389/fmicb.2025.1541140.
4. Liang B, Yuan Y, Peng XJ, Liu XL, Hu XK, Xing DM. Current and future perspectives for Helicobacter pylori treatment and management: From antibiotics to probiotics. Front Cell Infect Microbiol. 2022;12:1042070. doi: 10.3389/fcimb.2022.1042070.
5. Schulz C, Liou JM, Alboraie M, Bornschein J, Campos Nunez C, Coelho LG, Quach DT, Fallone CA, Chen YC, Gerhard M, Gisbert JP, Jung HY, Katelaris PH, Kim JG, Lu H, Macke L, Mahachai V, Moss SF, Remes-Troche JM, Riquelme A, Romano M, Setshedi M, Smith S, Suerbaum S, Tshibangu-Kabamba E, Vilaichone RK, Yadegar A, Yamaoka Y, Mégraud F, El-Omar EM, Sugano K, Malfertheiner P. Helicobacter pylori antibiotic resistance: A global challenge in search of solutions. Gut. 2025;74(10):1561-70. doi: 10.1136/gutjnl-2025-335523.
6. Suresh V, Sreekumar A, Kumar A, Sadasivan S, Biswas R, Biswas L. Therapeutic advances and future directions in Helicobacter pylori eradication. Front Microbiol. 2025;16:1652943. doi: 10.3389/fmicb.2025.1652943.
7. Follmer C. Ureases as a target for the treatment of gastric and urinary infections. J Clin Pathol. 2010;63(5):424-30. doi: 10.1136/jcp.2009.072595.
8. Cunha ES, Chen X, Sanz-Gaitero M, Mills DJ, Luecke H. Cryo-EM structure of Helicobacter pylori urease with an inhibitor in the active site at 2.0 Å resolution. Nat Commun. 2021;12(1):230. doi: 10.1038/s41467-020-20485-6.
9. Konieczna I, Żarnowiec P, Kwinkowski M, Koleśińska B, Frączyk J, Kamiński Z, Kaca W. Bacterial urease and its role in long-lasting human diseases. Curr Protein Pept Sci. 2012;13(8):789-806. doi: 10.2174/138920312804871094.
10. Tzvetkov NT, Atanasov AG. Natural product-based multitargeted ligands for Alzheimer's disease treatment? Future Med Chem. 2018;10(15):1745-8. doi: 10.4155/fmc-2018-0146.
11. Campos KR, Coleman PJ, Alvarez JC, Dreher SD, Garbaccio RM, Terrett NK, Tillyer RD, Truppo MD, Parmee ER. The importance of synthetic chemistry in the pharmaceutical industry. Science. 2019;363(6424):eaat0805. doi: 10.1126/science.aat0805.
12. Atanasov AG, Zotchev SB, Dirsch VM, Supuran CT. Natural products in drug discovery: Advances and opportunities. Nat Rev Drug Discov. 2021;20(3):200-216. doi: 10.1038/s41573-020-00114-z.
13. Newman DJ, Cragg GM. Natural products as sources of new drugs over the nearly four decades from 01/1981 to 09/2019. J Nat Prod. 2020;83(3):770-803. doi: 10.1021/acs.jnatprod.9b01285.
14. Xiao ZP, Wang XD, Peng ZY, Huang S, Yang P, Li QS, Zhou LH, Hu XJ, Wu LJ, Zhou Y, Zhu HL. Molecular docking, kinetics study, and structure-activity relationship analysis of quercetin and its analogues as Helicobacter pylori urease inhibitors. J Agric Food Chem. 2012;60(42):10572-7. doi: 10.1021/jf303393n.
15. Uddin G, Ismail, Rauf A, Raza M, Khan H, Nasruddin, Khan M, Farooq U, Khan A, Arifullah. Urease inhibitory profile of extracts and chemical constituents of Pistacia atlantica ssp. cabulica Stocks. Nat Prod Res. 2016;30(12):1411-6. doi: 10.1080/14786419.2015.1062378.
16. Asadi GS, Abdizadeh R, Abdizadeh T. Investigation of a set of flavonoid compounds as Helicobacter pylori urease inhibitors: Insights from *in-silico* studies. J Biomol Struct Dyn. 2025;43(5):2366-88. doi: 10.1080/07391102.2023.2295973.
17. Yu XD, Xie JH, Wang YH, Li YC, Mo ZZ, Zheng YF, Su JY, Liang YE, Liang JZ, Su ZR, Huang P. Selective antibacterial activity of patchouli

alcohol against Helicobacter pylori based on inhibition of urease. Phytother Res. 2015;29(1):67-72. doi: 10.1002/ptr.5227.
18. Lekmine S, Benslama O, Bensalah B, Touzout N, Moussa H, Tahraoui H, Ola MS, Hafsa H, Zhang J, Amrane A. Bioactive phenolics of Hyoscyamus muticus L. subsp. falezlez: A molecular and biochemical approach to antioxidant and urease inhibitory activities. Int J Mol Sci. 2025;26(1):370. doi: 10.3390/ijms26010370.
19. Yuan J, Li T, Gao S, Tang Y, Ma S, Lee HY, Chin KL, Xuan H. Mechanistic insights into Helicobacter pylori urease inhibition by poplar propolis ethanol extract. J Ethnopharmacol. 2026;365:121596. doi: 10.1016/j.jep.2026.121596.
20. Malekzadeh F, Ehsanifar H, Shahamat M, Levin M, Colwell RR. Antibacterial activity of black myrobalan (Terminalia chebula Retz.) against Helicobacter pylori. Int J Antimicrob Agents. 2001;18(1):85-88. doi: 10.1016/s0924-8579(01)00352-1.
21. Matsubara S, Shibata H, Ishikawa F, Yokokura T, Takahashi M, Sugimura T, Wakabayashi K. Suppression of Helicobacter pylori-induced gastritis by green tea extract in Mongolian gerbils. Biochem Biophys Res Commun. 2003;310(3):715-9. doi: 10.1016/j.bbrc.2003.09.066.
22. Tang Y, Yang F, Wen X, Zhou Y, Tang R, He X, Lu Q, Li C. Component characterization of Smilax glabra Roxb. and its inhibitory activity against Helicobacter pylori through targeted suppression of its secreted urease. Front Cell Infect Microbiol. 2025;15:1617330. doi: 10.3389/fcimb.2025.1617330.
23. Lionta E, Spyrou G, Vassilatis DK, Cournia Z. Structure-based virtual screening for drug discovery: Principles, applications and recent advances. Curr Top Med Chem. 2014;14(16):1923-38. doi: 10.2174/1568026614666140929124445.
24. Lipinski CA. Lead- and drug-like compounds: The rule-of-five revolution. Drug Discov Today Technol. 2004;1(4):337-41. doi: 10.1016/j.ddtec.2004.11.007.
25. Kumar M, Prachi P, Mehmood Z, Sharma P, Das R, Das K, Mahant S. Exploring an Indian herb Sphaeranthus indicus for antimicrobial efficacy against Helicobacter pylori and effect of combination therapy against drug resistant human pathogens. Int J Pharm Sci Med. 2021;6:51-74. doi: 10.47760/ijpsm.2021.v06i01.005.
26. Dinat S, Orchard A, Van Vuuren S. Antimicrobial activity of Southern African medicinal plants on Helicobacter pylori and Lactobacillus species. J Ethnopharmacol. 2024;330:118238. doi: 10.1016/j.jep.2024.118238.
27. Arun M, Asha VV. Gastroprotective effect of Dodonaea viscosa on various experimental ulcer models. J Ethnopharmacol. 2008;118(3):460-5. doi: 10.1016/j.jep.2008.05.026.
28. Wang YC. Medicinal plant activity on Helicobacter pylori-related diseases. World J Gastroenterol. 2014;20(30):10368-82. doi: 10.3748/wjg.v20.i30.10368.
29. Daina A, Michielin O, Zoete V. SwissADME: A free web tool to evaluate pharmacokinetics, drug-likeness and medicinal chemistry friendliness of small molecules. Sci Rep. 2017;7:42717. doi: 10.1038/srep42717.
30. Daina A, Zoete V. A BOILED-Egg to predict gastrointestinal absorption and brain penetration of small molecules. ChemMedChem. 2016;11(11):1117-21. doi: 10.1002/cmdc.201600182.
31. Trott O, Olson AJ. AutoDock Vina: Improving the speed and accuracy of docking with a new scoring function, efficient optimization, and multithreading. J Comput Chem. 2010;31(2):455-61. doi: 10.1002/jcc.21334.
32. Morris GM, Huey R, Lindstrom W, Sanner MF, Belew RK, Goodsell DS, Olson AJ. AutoDock4 and AutoDockTools4: Automated docking with selective receptor flexibility. J Comput Chem. 2009;30(16):2785-91. doi: 10.1002/jcc.21256.
33. Pires DEV, Blundell TL, Ascher DB. pkCSM: Predicting small-molecule pharmacokinetic and toxicity properties using graph-based signatures. J Med Chem. 2015;58(9):4066-72. doi: 10.1021/acs.jmedchem.5b00104.
34. Parr RG, Yang W. Density-functional theory of atoms and molecules. New York: Oxford University Press; 1995. doi: 10.1093/oso/9780195092769.001.0001.
35. Bowers KJ, Chow E, Xu H, Dror RO, Eastwood MP, Gregersen BA, Klepeis JL, Kolossváry I, Moraes MA, Sacerdoti FD, Salmon JK, Shan Y, Shaw DE. Scalable algorithms for molecular dynamics simulations on commodity clusters. In: Proceedings of the 2006 ACM/IEEE Conference on Supercomputing; 2006. p. 43. doi: 10.1109/SC.2006.54.
36. Shinu P, Sharma M, Gupta GL, Mujwar S, Kandeel M, Kumar M, Nair AB, Goyal M, Singh P, Attimarad M, Venugopala KN, Nagaraja S, Telsang M, Aldhubiab BE, Morsy MA. Computational design, synthesis, and pharmacological evaluation of naproxen-guaiacol chimera for gastro-sparing anti-inflammatory response by selective COX-2 inhibition. Molecules. 2022;27(20):6905. doi: 10.3390/molecules27206905.
37. Veber DF, Johnson SR, Cheng HY, Smith BR, Ward KW, Kopple KD. Molecular properties that influence the oral bioavailability of drug candidates. J Med Chem. 2002;45(12):2615-23. doi: 10.1021/jm020017n.
38. Lipinski CA. Drug-like properties and the causes of poor solubility and poor permeability. J Pharmacol Toxicol Methods. 2000;44(1):235-49. doi: 10.1016/S1056-8719(00)00107-6.
39. O'Donovan DH, De Fusco C, Kuhnke L, Reichel A. Trends in molecular properties, bioavailability, and permeability across the Bayer compound collection. J Med Chem. 2023;66(4):2347-60. doi: 10.1021/acs.jmedchem.2c01577.
40. Sadybekov AV, Katritch V. Computational approaches streamlining drug discovery. Nature. 2023;616(7958):673-85. doi: 10.1038/s41586-023-05905-z.

HOW TO CITE THIS ARTICLE: Keshav, Kaur M, Grewal AS. Docking-Guided Identification of Natural Urease Inhibitors Against *Helicobacter pylori*: Integrated ADME, Molecular Dynamics, and DFT Investigations. Int. J. Pharm. Sci. Drug Res. 2026;18(4):191-218. DOI: 10.25004/IJPSDR.2026.180403